

**From cyclic sand ratcheting to tilt accumulation of offshore monopiles
3D FE modelling using SANISAND-MS**

Liu, H.Y.; Kementzetzidis, E.; Abell, J. A.; Pisano, F.

DOI

[10.1680/jgeot.20.P.029](https://doi.org/10.1680/jgeot.20.P.029)

Publication date

2021

Document Version

Accepted author manuscript

Published in

Géotechnique

Citation (APA)

Liu, H. Y., Kementzetzidis, E., Abell, J. A., & Pisano, F. (2021). From cyclic sand ratcheting to tilt accumulation of offshore monopiles: 3D FE modelling using SANISAND-MS . *Géotechnique*, 72(9), 753-768. <https://doi.org/10.1680/jgeot.20.P.029>

Important note

To cite this publication, please use the final published version (if applicable).
Please check the document version above.

Copyright

Other than for strictly personal use, it is not permitted to download, forward or distribute the text or part of it, without the consent of the author(s) and/or copyright holder(s), unless the work is under an open content license such as Creative Commons.

Takedown policy

Please contact us and provide details if you believe this document breaches copyrights.
We will remove access to the work immediately and investigate your claim.

From cyclic sand ratcheting to tilt accumulation of offshore monopiles: 3D FE modelling using SANISAND-MS

H. Y. LIU*, E. KEMENTZETZIDIS†, J. A. ABELL‡, F. PISANÒ‡

Serviceability criteria for offshore monopiles include the estimation of long-term, permanent tilt under repeated operational loads. In the lack of well-established analysis methods, experimental and numerical research has been carried out in the last decade to support the fundamental understanding of monopile-soil interaction mechanisms, and the conception of engineering methods for monopile tilt predictions. With focus on the case of monopiles in sand, this work shows how step-by-step/implicit, three-dimensional finite element modelling can be fruitfully applied to the analysis of cyclic monopile-soil interaction and related soil deformation mechanisms. To achieve adequate simulation of cyclic sand ratcheting and densification around the pile, the SANISAND-MS model recently proposed by Liu *et al.* (2019b) is adopted. The link between local soil behaviour and global monopile response to cyclic loading is discussed through detailed analysis of model prediction. Overall, the results of numerical parametric studies confirm that the proposed 3D FE modelling framework can reproduce relevant experimental evidence about monopile-soil interaction, and support future improvement of engineering design methods.

KEYWORDS: offshore wind, monopile, cyclic loading, tilt, constitutive modelling, finite element modelling

INTRODUCTION

1 The offshore wind energy sector is rapidly expanding
2 worldwide (Tsai *et al.*, 2016; Mattar & Borvarán, 2016; Archer
3 *et al.*, 2017; Chancham *et al.*, 2017). Recent technological
4 advances have supported the growth in size and power output
5 of offshore wind turbines (OWTs), as well as the reduction of
6 fabrication and installation costs. Moving towards deeper and
7 harsher waters poses significant technical challenges, especially
8 regarding support structures and foundations. At present, most
9 OWTs are founded on monopiles, which are tubular steel
10 piles of large diameter and low embedment ratio (embedded
11 length/diameter, $\sim 3 - 6$). Due to the large costs for materials
12 and installation, the optimisation of foundation design is key to
13 cost-effective offshore wind developments.

14 Monopile design is mostly driven by the following criteria
15 (Bhattacharya, 2019):

- 16 1. first resonance frequency of the turbine-foundation-soil
17 system to lie within prescribed limits ('soft-stiff' range);
- 18 2. sufficient resistance to structural fatigue under prolonged
19 operational loads;
- 20 3. sufficient capacity under loads of exceptional magnitude;

4. full serviceability, i.e. limited deformations, under any
environmental and/or mechanical loads. 21 22

Regarding the fourth criterion, it is of special interest to avoid
in the long term excessive accumulation of rotation/deflection
under repeated loading. Specifically, some OWT manufacturers
prescribe that permanent OWT-monopile tilt should not exceed
 $\sim 0.5^\circ$ over the whole operational life, also including some
deviation from perfect verticality after installation (Arany *et al.*,
2015). In the lack of well-established calculation procedures,
intensive work has been carried out to explain and quantify
geotechnical mechanisms governing monopile tilt under lateral
cyclic loading (Houlsby, 2016). The tilting response of
monopile results overall from the interplay of several factors,
such as loading conditions, soil type and behaviour, geometry
and mechanical properties of the foundation. 23 24 25 26 27 28 29 30 31 32 33 34 35

Significant experimental work has been devoted in the last
decade to the study of monopile tilt under high-cyclic lateral
loading, mostly for the case of sandy soils under drained
conditions (i.e., without accounting for pore pressure effects)
– see the recent overviews provided, e.g., by Truong *et al.*
(2019) and Page *et al.* (2020). As for numerical modelling
research, the intrinsic complexity of the problem has promoted
the development of simplified analysis methods. In particular,
the following approaches for numerical tilt predictions have
gained broadest popularity: 36 37 38 39 40 41 42 43 44 45

- methods based on '0D' modelling of monopile-soil
interaction. In this approach, distributed/continuum
geotechnical mechanisms are lumped into a single
macro-element formulated in terms of only a few pairs 46 47 48 49

Manuscript received...

* Department of Offshore Energy - Advanced Modelling Section, Norwegian Geotechnical Institute, 0806, Oslo, Norway (formerly Delft University of Technology)

† Facultad de Ingeniería y Ciencias Aplicadas, Universidad de los Andes, Mons. Alvaro del Portillo 12.455, 762000111, Las Condes, Santiago, Chile

‡ Faculty of Civil Engineering and Geoscience, Delft University of Technology, Stevinweg 1, 2628 CN Delft, The Netherlands

(six at most) of generalised static (forces/moments) and kinematic (displacement/rotations) variables (Houlsby *et al.*, 2017; Abadie *et al.*, 2019b). Non-linear monopile macro-elements have also been used to account for soil-foundation interaction effects in the dynamic analysis of OWTs (Page *et al.*, 2019), and may potentially be extended to tackle cyclic loading conditions (di Prisco & Pisanò, 2011);

- methods based on 3D soil-foundation modelling and simulation of the ‘local’ soil response around the foundation. While space discretisation is usually performed through the finite element (FE) method, time marching can be tackled according to two distinct approaches – either ‘explicit’ or ‘implicit’, in the terminology used by Niemunis *et al.* (2005).

In the explicit framework, accumulated strains are explicitly linked to the number of loading cycles N , so that relevant components of accumulated strain are calculated at all soil locations only at one selected time for each loading cycle. Owing to their relatively low computational costs, explicit methods have been already applied by several authors to the 3D FE analysis of cyclically loaded monopiles (Achmus *et al.*, 2009; Jostad *et al.*, 2014; Wichtmann *et al.*, 2017; Chong, 2017; Staubach & Wichtmann, 2020). Explicit models rely on extensive laboratory testing programmes, and build on the translation of cyclic loading histories into sequences of N -driven monotonic steps. In contrast, the implicit approach is more ‘conventional’ in that it encompasses the simulation of cyclic soil behaviour as a causal sequence of stress/strain increments, to be integrated in the time domain (step-by-step integration). To date, 0D-implicit and 3D-explicit approaches have been preferred to implicit 3D simulations – so far only rarely applied to monopile tilt problems (Barari *et al.*, 2017; Sheil & McCabe, 2017). Nonetheless, implicit 3D FE modelling appears to possess higher potential to explain/predict governing geo-mechanisms (Pisanò, 2019; Jostad *et al.*, 2020; Liu, 2020; Cheng *et al.*, 2021), and is being increasingly adopted to study the cyclic/dynamic performance of OWT-monopile-soil systems (Cuéllar *et al.*, 2014; Kementzetzidis *et al.*, 2018, 2019, 2020). Furthermore, it is envisaged that implicit approaches may support in the near future the refinement of existing explicit models, for instance with regard to the cyclic evolution of phenomenological/non-measurable variables adopted in implicit constitutive models. The two approaches could eventually be combined to set a path from experimental observations to engineering predictions that passes through a stage of more detailed (implicit) modelling. Such a stage would allow the generalisation of laboratory data to conditions not directly tested, and ultimately the improvement of empirical/explicit laws.

At the present state of the art, performing sound 3D FE calculations is still challenging for the following reasons:

- cyclic deformations develop in the soil under the influence of numerous factors. The influence of the loading history and soil microstructure is by now well acknowledged (Park & Santamarina, 2019; Gao & Meguid, 2018)
- numerical approximation errors are inevitably produced during the time integration of stress/strain increments in each loading cycle. As a consequence, numerical errors might accumulate in the presence of a large number of cycles (Niemunis *et al.*, 2005), depending on the adopted stress point integration strategy;
- the need for accurate time integration over numerous loading cycles makes implicit 3D FE modelling computationally demanding. This issue is particularly apparent for OWT foundation problems, which can involve up to 10^7 - 10^8 operational cycles.

This study highlights the benefits of implicit 3D FE modelling in relation to the tilting analysis of monopiles in sand. Such a goal is pursued through the application of SANISAND-MS, a constitutive model recently proposed by Liu *et al.* (2019b) to enhance the simulation of high-cyclic sand ratcheting (Wichtmann, 2005; di Prisco & Mortara, 2013), and therefore the assessment of foundation serviceability under cyclic loading. Following recent constitutive modelling work (Liu *et al.*, 2019b; Liu & Pisanò, 2019; Liu *et al.*, 2020), SANISAND-MS is here adopted for the first time to tackle a 3D boundary value problem.

It is worth recalling that a thorough validation process should include quantitative comparison between the results of pile loading tests and corresponding 3D FE simulations, with the latter to be performed using soil parameters calibrated against soil laboratory data. However, the experimental literature does not yet sufficiently support to such endeavor, since it is still difficult to access pile test results obtained after thorough (high-)cyclic characterisation (Truong *et al.*, 2019; Richards *et al.*, 2019). Therefore, an alternative approach was followed to achieve a semi-quantitative validation of the considered framework. 3D FE simulations of an average’ full-scale monopile were performed by using SANISAND-MS parameters identified by Liu *et al.* (2019b) for a sand extensively tested in Karlsruhe (Wichtmann, 2005). After detailed inspection of the numerical results, simulated trends of cyclic monopile tilt were semi-quantitatively’ compared to experimental data from the literature. As a first take on the subject, the scope of this paper is limited to the case of a monopile ‘wished-in-place’ in dry sand and subjected to unidirectional lateral loading, with emphasis on the interplay of cyclic loading and sand density conditions in determining the permanent tilt of the reference monopile.

SANISAND-MS MODEL

This section summarises key aspects of the SANISAND-MS model, which was recently proposed to improve the simulation

153 of cyclic sand behaviour (Liu *et al.*, 2019b; Liu & Pisanò, 2019)
 154 with regard to drained high-cyclic ratcheting and related strain
 155 accumulation (Wichtmann, 2005). As this paper exclusively
 156 addresses the case of a monopile in dry sand, the application of
 157 SANISAND-MS to hydro-mechanical coupled problems was
 158 not attempted, although recently tackled from a constitutive
 159 modelling perspective (Liu *et al.*, 2018, 2019a, 2020).

160 SANISAND-MS' bounding surface formulation builds on
 161 the parent SANISAND2004 model developed by Dafalias &
 162 Manzari (2004), with the addition of a so-called 'memory
 163 surface' in replacement of the fabric tensor (Corti *et al.*, 2016).

164 The model adopts a critical state framework with four
 165 relevant loci (Fig. 1): (1) a narrow conical yield locus (f),
 166 enclosing the elastic domain; (2) a wide conical bounding
 167 surface (f^B), setting current stress bounds consistent with an
 168 evolving state parameter (Been & Jefferies, 1985), as proposed
 169 by Manzari & Dafalias (1997); (3) a conical dilatancy surface
 170 (f^D), separating stress zones associated with contractive
 171 and dilative deformations (Manzari & Dafalias, 1997; Li &
 172 Dafalias, 2000; Dafalias & Manzari, 2004); (4) a conical
 173 memory surface (f^M), bounding an evolving stress region
 174 associated with non-virgin loading, and therefore related to
 175 the evolution of stress-induced anisotropy at the micro-scale.
 176 The memory surface allows a phenomenological representation
 177 of micro-mechanical effects associated with fabric changes
 178 occurring during cycling, such as variations in stiffness and
 179 dilatancy. Such changes possess at the micro-scale both
 180 intensity' and directionality' attributes, which inspired the
 181 introduction in SANISAND-MS of a combined isotropic-
 182 kinematic hardening mechanism for the memory surface (Corti
 183 *et al.*, 2016; Liu *et al.*, 2019b).

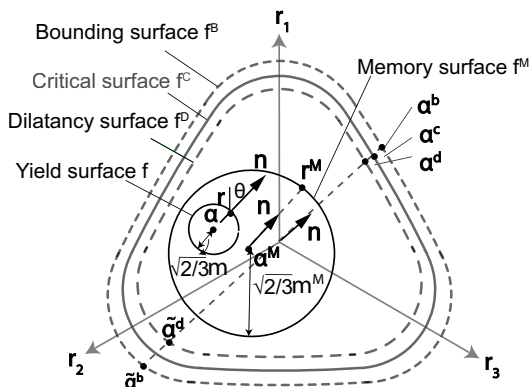


Fig. 1. SANISAND-MS model loci in the deviatoric stress ratio plane.

184 The evolution of elasto-plastic sand stiffness is governed
 185 in SANISAND-MS both by the bounding and the memory
 186 surfaces through the plastic modulus K_p :

$$K_p = \frac{2}{3}ph(\alpha^b - \alpha) : \mathbf{n} \quad (1)$$

187 where $(\alpha^b - \alpha) : \mathbf{n}$ quantifies the distance between the back-
 188 stresses associated with bounding and yield surfaces (α^b and

α), after projection along the direction of \mathbf{n} (unit tensor normal
 to the yield surface). The hardening coefficient h is defined as:

$$h = \frac{b_0}{(\alpha - \alpha_{in}) : \mathbf{n}} \exp \left[\mu_0 \left(\frac{p}{p_{atm}} \right)^{0.5} \left(\frac{b^M}{b_{ref}} \right)^2 \right] \quad (2)$$

191 with $b^M = (\mathbf{r}_\alpha^M - \alpha) : \mathbf{n}$ accounting for the distance between
 192 memory and yield loci, $\mathbf{r}_\alpha^M = \alpha^M + \sqrt{2/3}(m^M - m)\mathbf{n}$, and
 193 $b_{ref} = (\alpha^b - \alpha^b) : \mathbf{n}$ – with all terms defined as shown in Fig.
 194 1. m^M and m are related to the radii of memory and yield
 195 surface, respectively, b_0 is a factor depending on the current
 196 void ratio and mean effective stress, while μ_0 is a model
 197 parameter governing strain accumulation (ratcheting) under
 198 drained cyclic loading. At variance with the first SANISAND-
 199 MS formulation (Liu *et al.*, 2019b), the yield back-stress ratio
 200 α and its projections onto bounding (α^b), dilatancy (α^d), and
 201 critical (α^c) surfaces are used here as in SANISAND2004 –
 202 see Liu & Pisanò (2019) and Liu (2020).

203 Experimental observations inspired the evolution laws
 204 assumed for the back-stress α^M and size m^M of the memory
 205 surface (Liu *et al.*, 2019b). As contractive behaviour promotes
 206 'fabric reinforcement', stages of cyclic contraction are linked to
 207 an expansion of the memory surface ($dm^M > 0$), and therefore
 208 to larger stiffness through Eqs. (1)–(2). An additional memory-
 209 shrinking mechanism ($dm^M < 0$) was also deemed necessary
 210 to simulate the loss in stiffness caused by stages of dilative
 211 deformation. The proposed incremental law for the memory
 212 surface size is expressed as follows:

$$dm^M = \sqrt{\frac{3}{2}} d\alpha^M : \mathbf{n} - \frac{m^M}{\zeta} f_{shr} \langle -d\varepsilon_v^p \rangle \quad (3)$$

213 where f_{shr} is a geometrical shrinkage factor defined in Liu
 214 *et al.* (2019b), while ζ is a material parameter governing the
 215 shrinkage rate of the memory surface during dilation. The
 216 kinematics of the memory back-stress α^M follows directly
 217 from a parallel consistency condition imposed with respect to
 218 the memory surface:

$$d\alpha^M = 2/3 \langle \Lambda \rangle h^M (\alpha^b - \mathbf{r}_\alpha^M) \quad (4)$$

219 Compared to SANISAND2004, the formulation of the
 220 dilatancy coefficient D was slightly modified by adding a
 221 memory-related factor able to enhance sand contractancy after
 222 stages of dilative deformation – such a phenomenon is often
 223 associated with so-called 'fabric re-orientation'. Further details
 224 about constitutive formulation and parameter calibration are
 225 available in Liu *et al.* (2019b) and Liu (2020).

226 All the 3D FE results presented in this paper were obtained
 227 using reference SANISAND-MS parameters for the Karlsruhe
 228 sand, which is a medium-coarse quartz sand featuring the index
 229 properties reported in Table 1 (Wichtmann, 2005). Karlsruhe
 230 sand's SANISAND-MS parameters were previously calibrated

Table 1. Karlsruhe sand's index properties – after Wichtmann (2005)

min/max void ratio	min/max dry unit weight	median particle diameter	uniformity coefficient
$e_{min,max}$	$\gamma_{min,max}$	D_{50}	C_u
0.577 – 0.874	13.9 – 16.5 kN/m ³	0.55 mm	1.8

Table 2. Karlsruhe sand's SANISAND-MS model parameters – after Liu et al. (2019b).

Elasticity		Critical state					Yield surface	Plastic modulus			Dilatancy		Memory surface		
G_0	ν	M_c	c	λ_c	e_0	ξ	m	h_0	c_b	n^b	A_0	n^d	μ_0	ζ	β
110	0.05	1.27	0.712	0.049	0.845	0.27	0.01	5.95	1.01	2.0	1.06	1.17	260	0.0005	1

231 by Liu et al. (2019b) against the results of single-amplitude
 232 high-cyclic triaxial tests (10^4 cycles) – see Table 2.

3D FE MODELLING OF MONOPILE-SOIL INTERACTION

233 Monopile-soil interaction analyses were carried out using
 234 the 3D FE modelling capabilities available in OpenSees
 235 (sequential version) (McKenna, 2011). Such capabilities were
 236 enhanced with an implementation of SANISAND-MS built
 237 on the existing SANISAND2004 code from the University of
 238 Washington (Ghofrani & Arduino, 2018). This section covers
 239 the setup of the reference 3D FE model (see also Corciulo
 240 et al. (2017) and Taborda et al. (2019)), while its accuracy is
 241 discussed in the final Appendix.

Soil and monopile

242 Fig. 2 displays the monopile-soil model adopted in this work,
 243 which includes:

- 245 – an elastic tubular monopile, with diameter, embedded
 246 length and wall thickness representative of typical full-
 247 scale monopiles and equal to $D = 5$ m, $L = 20$ m, and
 248 $t = 10$ cm, respectively;
- 249 – a soil domain with dimensions $[W_1, W_2, L + B] =$
 250 $[30\text{m}, 35\text{m}, 30\text{m}]$ (Fig. 2). Such dimensions are sufficient
 251 to avoid domain boundary effects on the lateral response
 252 of the pile, as previously shown by Corciulo et al. (2017).
 253 As the following discussion refers to mono-directional
 254 lateral loading, only half domain was modelled for
 255 computational convenience;
- 256 – lateral loading applied with an eccentricity $e_{ecc} = L =$
 257 20 m above the soil surface. Such a value is consistent
 258 with e_{ecc}/L ratios set in relevant small-scale testing
 259 studies (e.g., $e_{ecc} \approx 1.2L$ in LeBlanc et al. (2010)), even
 260 though (variable) eccentricities in excess of $4L$ may
 261 apply to real field conditions (McAdam et al., 2019). The
 262 load application point was connected to the 3D pile head
 263 at the mudline through an elastic Timoshenko beam.

264 Boundary conditions were imposed on the soil domain to
 265 obtain fully fixed bottom surface, free upper surface, and no
 266 horizontal displacement along the direction perpendicular to
 267 the lateral surface. Both the soil and the embedded monopile
 268 were discretised using 8-node, one-phase SSP brick elements,
 269 featuring a stabilised, single-point formulation already proven

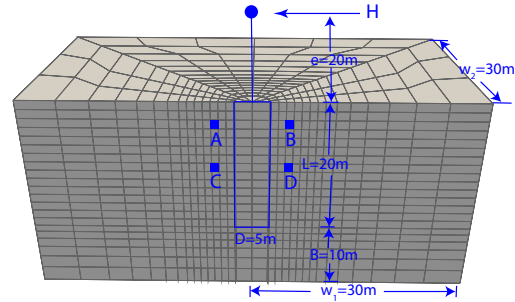


Fig. 2. FE model domain. The reference soil elements (A, B, C, D) are located 2.7 m (A and B) and 9.3 m (C and D) under the ground surface, at a distance of 2.1 m from the monopile shaft.

270 effective against shear/volumetric locking issues in elasto-
 271 plastic media (McGann et al., 2015). Non-linear static
 272 simulations of cyclic pile loading were performed using
 273 implicit time integration, with iterative solution of each step
 274 based on the Krylov–Newton algorithm described by Scott &
 275 Fenves (2003). Each (sinusoidal) load cycle was partitioned
 276 into 60 step increments, with global convergence tested against
 277 a relative error tolerance of 10^{-3} on the displacement solution
 278 vector. SANISAND-MS constitutive equations were integrated
 279 in time at individual stress points using an explicit, fourth-order
 280 Runge-Kutta (RK) algorithm, featuring automatic error control
 281 and sub-stepping (Sloan, 1987; Tamagnini et al., 2000; Sloan
 282 et al., 2001). RK stress integration requires the input of separate
 283 tolerances for plasticity activation and sub-stepping, which
 284 were set to $F\text{TOL} = 10^{-4}$ kPa (computed value of the yield
 285 function) and $S\text{TOL} = 10^{-4}$ (dimensionless), respectively –
 286 see Appendix.

287 While the SANISAND-MS parameters in Table 2 were
 288 adopted for the soil (Wichtmann, 2005; Liu et al., 2019b),
 289 typical values of Young's modulus ($E_{steel} = 221\text{GPa}$) and
 290 Poisson's ratio ($\nu_{steel} = 0.3$) were set for the monopile steel.
 291 Following the simplified approach by Griffiths (1985), the pile-
 292 sand interface was modelled by introducing around the pile
 293 a thin layer of soil bricks with 'degraded' SANISAND-MS
 294 properties, so as to heuristically reproduce possible installation
 295 effects – though without attempting to model soil-pile gapping
 296 during cyclic loading (Day & Potts, 1994; Cerfontaine et al.,
 297 2015). The interface layer in the final model was as thick as
 298 $\sim 1\%$ of the monopile diameter; its constitutive parameters
 299 were assumed to differ from those in Table 2 only in terms of

Table 3. Numerical simulation programme and corresponding T_b - T_c values inferred from FE results based on Eq. (6) with a single accumulation exponent ($\alpha = 0.5$).

Test label	D_r	ζ_b	ζ_c	T_b	T_c	Test label	D_r	ζ_b	ζ_c	T_b	T_c
L1	30%	0.5	0	0.1	1	D1	70%	0.5	0	0.2	1
L2	30%	0.3	0	0.08	1	D2	70%	0.3	0	0.12	1
L3	30%	0.1	0	0.06	1	D3	70%	0.1	0	0.045	1
L4	30%	0.05	0	0.04	1	D4	70%	0.05	0	0.026	1
L5	30%	0.025	0	0.022	1	D5	70%	0.025	0	0.017	1
L6	30%	0.0125	0	0.014	1	D6	70%	0.0125	0	0.01	1
L7	30%	0.3	0.7	0.08	0.4	D7	70%	0.3	0.7	0.12	0.3
L8	30%	0.3	0.5	0.08	0.6	D8	70%	0.3	0.5	0.12	0.6
L9	30%	0.3	0.3	0.08	0.8	D9	70%	0.3	0.3	0.12	0.8
L10	30%	0.3	-0.25	0.08	1.1	D10	70%	0.3	-0.25	0.12	1.2
L11	30%	0.3	-0.5	0.08	0.8	D11	70%	0.3	-0.5	0.12	0.8
L12	30%	0.3	-0.75	0.08	0.5	D12	70%	0.3	-0.75	0.12	0.6

300 dimensionless shear modulus ($G_0 = 94$) and critical stress ratio
301 ($M_c = 0.96$).

302 Prior to the cyclic phase, stresses and internal variables in
303 the FE model were in all cases initialised through standard
304 gravity loading with the pile already ‘wished in place’ (WIP).
305 In particular, the memory surface was initially set to coincide
306 everywhere with yield surface, i.e., $m^M = m$ (cf. Eq. (3) to
307 Table 2). This is clearly a crude simplification of reality, in
308 that it excludes expected installation effects from the cyclic
309 response of the pile. In this respect, Staubach *et al.* (2020)
310 recently compared the cyclic tilt returned by ‘explicit’ 3D FE
311 analyses for monopiles either WIP or jacked/impact-driven,
312 with the latter cases studied via Coupled Eulerian-Lagrangian
313 simulations. The authors found WIP-based tilt predictions
314 on the conservative side, although further parametric studies
315 are certainly needed to corroborate such a conclusion. A
316 growing body of experimental research on this subject is
317 currently contributing to filling knowledge gaps related to pile
318 installation effects (Anusic *et al.*, 2019; Heins *et al.*, 2020;
319 Metrikine *et al.*, 2020).

320 Numerical simulation programme

321 Although non-stationary and multi-directional in nature
322 (Rudolph *et al.*, 2014; Richards *et al.*, 2019), only unidirectional
323 lateral loading applied in single-amplitude cycles was
324 considered in this first study. The core of this work’s FE
325 simulation programme relates to the cases listed in Table 3,
326 with two values of initial sand’s relative density, $D_r = 30\%$ and
327 70% . Such values were selected as representative of generally
328 loose and dense sand, though without trying to match specific
329 soil conditions in the selected reference experiments (see next
330 section). In all cases, the total number of cycles was limited to
331 $N = 100$, which resulted in a calculation time of approximately
332 49 hours on a computer equipped with an Intel Xeon W-
333 2125 cpu (processor base frequency: 4.0 GHz). The duration of
334 (sequential) 3D FE simulations was mostly affected by the
335 number/density of finite elements in the soil domain (Fig. 2),
336 the degree of soil non-linearity mobilised by the applied loads,
337 and the algorithmic settings in both global (Krylov–Newton)
338 and stress-point (RK) time integration – see Appendix.

339 The simulation programme in Table 3 was conceived to
340 investigate the influence of different (non-symmetric) cyclic

341 loading conditions on the cyclic tilt of monopiles. In particular,
342 minimum/maximum lateral load values (H in Fig. 2) were
343 selected to modify the amplitude and asymmetry of cyclic
344 loading according to the dimensionless load factors defined by
345 LeBlanc *et al.* (2010):

$$\zeta_b = \frac{H_{max}}{H_{ref}} = \frac{M_{max}}{M_{ref}} \quad (5)$$

$$\zeta_c = \frac{H_{min}}{H_{max}} = \frac{M_{min}}{M_{max}}$$

346 where H_{max} (M_{max}) and H_{min} (M_{min}) stand for maxi-
347 mum and minimum horizontal load (moment at mudline),
348 respectively. H_{ref} (M_{ref}) is the horizontal force (moment)
349 associated with a ‘conventional’ definition of lateral capacity,
350 here assumed to correspond with a lateral deflection of $0.1D$ at
351 the ground surface. Accordingly, H_{ref} values equal to 26800
352 kN and 15450 kN were determined through 3D FE calculations
353 for $D_r = 70\%$ and $D_r = 30\%$, respectively, and the same load
354 eccentricity in Fig. 2. Table 3 includes loading cases associated
355 both with one-way ($\zeta_c \geq 0$, positive H_{max} and H_{min}) and
356 (biased) two-way loading ($-1 \leq \zeta_c < 0$, positive H_{max} and
357 negative H_{min}).

SANISAND-MS 3D FE SIMULATION OF CYCLIC MONOPILE BEHAVIOUR

358 After some observations on the simulated pile response to
359 monotonic and two-way/symmetric loading, general features
360 of the 3D FE results associated with Table 3 are discussed
361 and broadly compared to selected 1g small-scale test data
362 from the literature, particularly those reported by LeBlanc
363 *et al.* (2010) and Richards *et al.* (2019) – see experimental
364 settings in Table 4. As different soil/pile/loading settings were
365 considered in numerical simulations and reference experiments,
366 the main goal is to verify whether SANISAND-MS can
367 generally reproduce expected features of cyclic sand-monopile
368 interaction. Nonetheless, the important difference related to the
369 total number of loading cycles in the reference experiments
370 (thousands) and 3D FE simulations (one hundred) should also
371 be borne in mind. In what follows, the term ‘pile head’ is always
372 used for brevity in lieu of ‘at the level of soil surface’.

Table 4. Specifications of selected 1g small-scale tests.

	Sand properties	Pile test settings
LeBlanc <i>et al.</i> (2010)	Yellow Leighton Buzzard 14/25 $D_{50,10}=0.81, 56$ $C_u=1.55$ $\gamma_{max,min}=17.64, 14.43 \text{ kN/m}^3$ $\phi_{cr}=34.3^\circ$	$L=360 \text{ mm}$ $D=80 \text{ mm}$ $t=2 \text{ mm}$ $e_{ecc}=430 \text{ mm}$
Richards <i>et al.</i> (2019)	Yellow Leighton Buzzard $D_{50,10}=0.8, 0.63 \text{ mm}$ $C_u=1.35$ $\gamma_{max,min}=17.58, 14.65 \text{ kN/m}^3$ $\phi_{cr}=34.3^\circ$	$L=320 \text{ mm}$ $D=80 \text{ mm}$ $t=5 \text{ mm}$ $e_{ecc}=800 \text{ mm}$

373 Monotonic behaviour

374 As a first step, the simulated monotonic behaviour of the
375 monopile was considered. Fig. 3 shows a comparison between
376 the monotonic responses obtained through 3D FE modelling and
377 reported by Achmus *et al.* (2020) after full-scale field tests. The
378 field data from Achmus *et al.* (2020) were considered suitable
379 for such a comparison in that they relate to two monopiles,
380 P3 and P4, of dimensions similar to those in the reference
381 numerical model, i.e., $D = 4.3 \text{ m}$ and $L = 18.5 \text{ m}$ (cf. to $D = 5$
382 m and $L = 20 \text{ m}$ in Fig. 2). Only for this monotonic loading
383 case, the load eccentricity in the FE model was reduced to 1
384 m above the ground surface, in order to match the setup in
385 Achmus *et al.*'s tests. The same Karlsruhe sand parameters in
386 Table 2 were retained, as it was not attempted to reproduce in
387 detail the behaviour of the 'medium to very dense sand' at the
388 site. Nevertheless, distinct FE simulations were performed for
389 the cases of dry and fully saturated sand ($D_r = 70\%$), so as to
390 highlight the impact of stress-dependent soil stiffness.

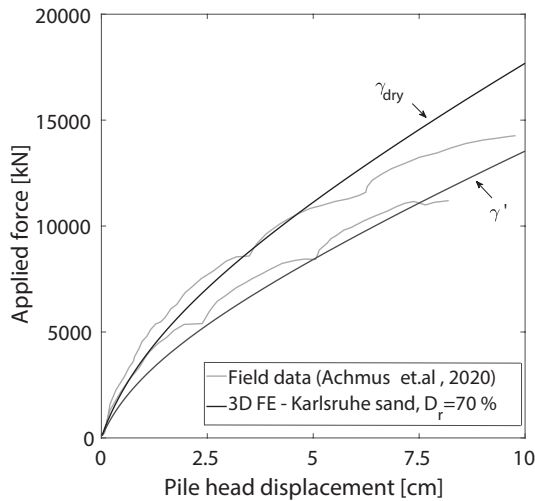


Fig. 3. Comparison between monotonic monopile responses from 3D FE modelling (Karlsruhe sand, $D_r = 70\%$ - $\gamma_{dry} = 15.3 \text{ kN/m}^3$ and $\gamma' = 9.4 \text{ kN/m}^3$) and field testing (from Achmus *et al.* (2020), piles P3-P4).

391 Despite of the differences in pile geometry, installation
392 method (WIP vs impact- and vibro-driven), and soil conditions,
393 the comparison in Fig. 3 confirms that the SANISAND-MS
394 3D FE model can produce monotonic pile responses in general
395 agreement with reality.

Behaviour under two-way/symmetric cyclic loading

396 Fig. 4 provides further insight into the SANISAND-MS FE
397 model performance with respect to two-way/symmetric cyclic
398 loading (i.e., with $\zeta_c = -1$). Fig. 4a shows the cyclic response
399 simulated for the reference monopile in dense Karlsruhe sand
400 ($D_r = 70\%$) under 25 loading cycles of different amplitude,
401 i.e., $\zeta_b = 0.1, 0.2, 0.4$. It is readily visible that, prior to reaching
402 a steady state, the pile experiences in all cases some net tilt,
403 alongside a gradual stiffening of the response cycles. A similar
404 response to symmetric cyclic loading has been very recently
405 reported by Richards *et al.* (2021) after centrifuge testing
406 at 80g (i.e., representative of a large-scale monopile). Even
407 in the case of an initially homogeneous system, symmetric
408 loading can gradually induce 'asymmetry' in sand's conditions
409 when applied laterally. Changes in sand fabric (and stiffness)
410 develop in the soil in a way specific to the loading sequence,
411 and therefore not synchronously/symmetrically around the pile.
412 This may be even more true in reality due to inevitable initial
413 inhomogeneities, which may in turn promote some net pile tilt
414 under symmetric loading. The extent of the pile tilt resulting
415 from SANISAND-MS FE simulations is not only a function of
416 the cyclic load amplitude, but also of the fabric-memory effects
417 that are inherent to the constitutive model. In the last respect,
418 Fig. 4a also shows the FE response obtained for $\zeta_b = 0.2$ after
419 inhibiting the memory surface mechanism in SANISAND-
420 MS (i.e., after setting $\mu_0 = \beta = 0$ in Table 2). It is readily
421 apparent that, in the absence of sand stiffening during cycling,
422 the cyclic response (i) reaches more quickly a steady state, and
423 (ii) exhibits only very limited net tilt under symmetric loading.
424 This occurrence underlines the importance of 'realistically'
425 initialising the memory surface locus (i.e., m^M and α^M in
426 Eqs. (3)-(4), for instance with respect to specific effects of
427 pile installation. It is anticipated that preliminary simulation of
428 the pile driving process could return distributions of m^M and
429 α^M that would potentially result in (more) realistic evolution
430 of monopile stiffness and tilt under cyclic loading.

431 It seems interesting to discuss whether the FE response to
432 symmetric loading complies, at the macroscale, with a typical
433 Masing-type representation. In Fig. 4b the steady cycles (black
434 solid lines, re-centred with respect to the (0;0)) from Fig. 4a
435 for different ζ_b values are plotted together with their closest
436 'Masing fitting' (black dashed lines). Even though bounding
437 surface models do not produce stress-strain response cycles
438 exactly compliant with Masing's idealisation (Borja & Amies,
439 1994), the simulated pile behaviour appears to match a Masing-
440 type response at the global scale, which is in agreement with
441 the experimental findings of Abadie *et al.* (2019a). However,
442 Fig. 4b also shows that the reference Masing cycles (black
443 dashed lines) could not be built on the initial/monotonic 3D
444 FE response branch (green line), but rather on stiffer branches
445 (magenta lines) that represent the lateral pile stiffness in
446 the last cycle applied with a specific load amplitude. This
447 fact is a consequence of the cyclic soil stiffening simulated
448

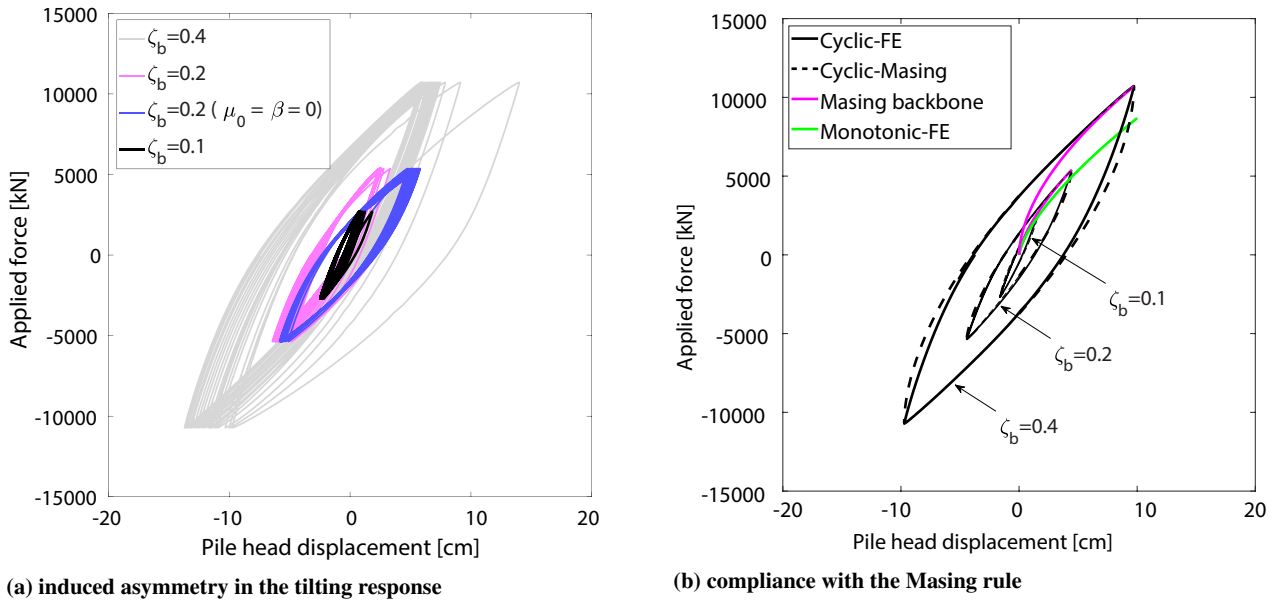


Fig. 4. Simulated monopile response to symmetric cyclic loading of different amplitude ($\zeta_b = 0.1, 0.2, 0.4$ and $D_r = 70\%$).

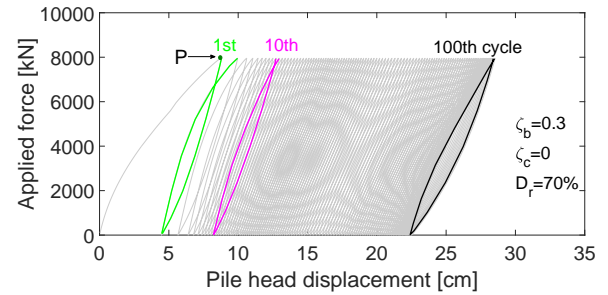
449 by SANISAND-MS through its memory surface hardening
450 mechanism (cf. to Fig. 4a).

451 Behaviour under one-way cyclic loading

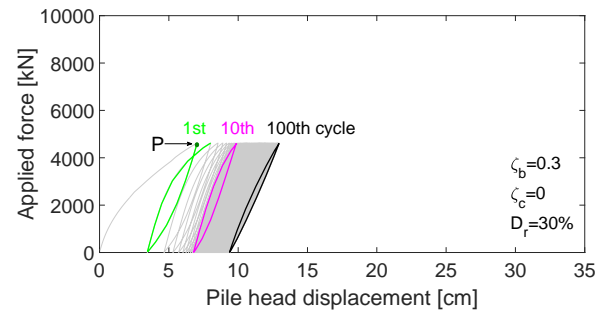
452 This subsection describes in more detail general response
453 features under one-way cyclic loading (i.e., with $\zeta_c \geq 0$), which
454 is most relevant to monopile tilting (Klinkvort, 2013). Typical
455 cyclic responses recorded at the pile head are plotted in Fig. 5
456 for the simulation cases D2 and L2 in Table 3. Figs. 5a and
457 5b clearly show that the pile head displacement induced by
458 the first monotonic loading (i.e., up to point P in the figures)
459 is (i) weakly affected by D_r (this is consistent with applying
460 a maximum loads of equal relative magnitude ζ_b), and (ii) is
461 significantly larger than the displacement produced within each
462 of the subsequent loading cycles. Displacement accumulation
463 can be observed to progress under cyclic loading at a gradually
464 decreasing rate. This kind of global ratcheting behavior appears
465 to be fully related to the local ratcheting exhibited by sand
466 samples during cyclic laboratory tests (Wichtmann, 2005; Liu
467 et al., 2019b).

468 Complementary visualisation of the pile tilting response
469 is provided in Fig. 5c in terms of accumulated displacement/
470 rotation against the number of cycles N . For given load
471 settings, the relative density has clearly a quantitative impact
472 on the accumulation of permanent pile rotation, as indicated by
473 available experimental data (LeBlanc et al., 2010).

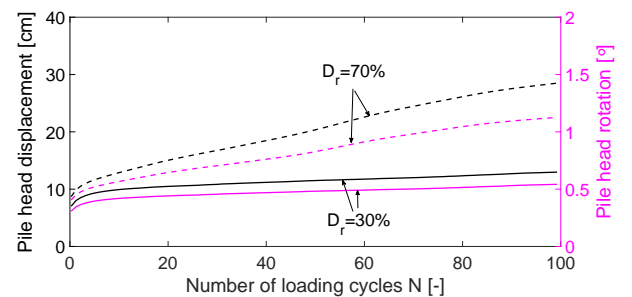
474 In this respect, it is common to plot rotation accumulation
475 trends after normalisation with respect to a reference rotation
476 θ_s defined by LeBlanc et al. (2010) as the rotation that
477 would occur in a static test when the load is equivalent
478 to the maximum cyclic load. Numerical results regarding
479 monopile tilt accumulation are displayed in the following in the
480 normalised $\Delta\theta/\theta_s$ form, where $\Delta\theta = \theta_N - \theta_0$ is the difference
481 between the rotation accumulated after N cycles (θ_N) and the



(a) Lateral force vs pile head displacement ($D_r = 70\%$)



(b) Lateral force vs pile head displacement ($D_r = 30\%$)



(c) Pile head displacement/rotation vs number of cycles

Fig. 5. Cyclic pile head response resulting from SANISAND-MS 3D FE simulations – simulation cases D2 and L2 in Table 3.

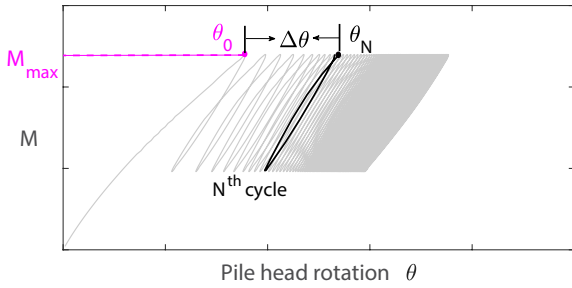


Fig. 6. Definition of reference pile rotation values.

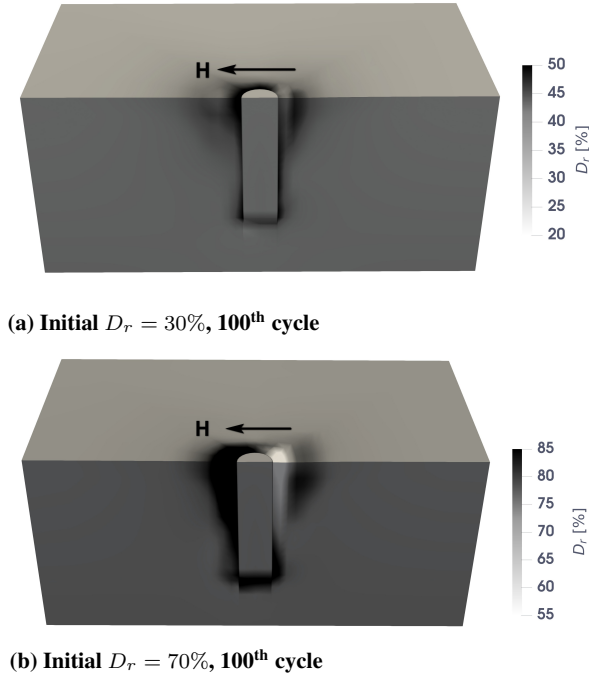


Fig. 7. Distribution of sand relative density (D_r) after 100 loading cycles – simulations cases L2 (a) and D2 (b) in Table 3.

482 rotation at the end of the pre-cycling monotonic phase (θ_0) (see
483 Fig. 6). Although θ_s and θ_0 may not exactly coincide when
484 obtained experimentally, it is accurate to assume $\theta_s = \theta_0$ within
485 the adopted modelling framework.

486 Each of the performed 3D FE analyses returned detailed
487 ‘numerical data’ about the cyclic response of sand during
488 pile loading, including the evolution of stresses, strains,
489 and all internal/hardening variables in the SANISAND-MS
490 formulation. For example, interesting indications are provided
491 by the pseudo-colour plots in Fig. 7, in which the relative
492 density distribution at the end of the 100th cycle is displayed
493 for the same cases L2 ($D_r = 30\%$) and D2 ($D_r = 70\%$). The
494 D_r plots in Fig. 7 confirm well-established evidence about
495 cyclic sand densification (Cuéllar *et al.*, 2009), e.g., regarding
496 D_r variations being relatively more pronounced in loose sand.
497 As the selected FE results refer to pure one-way loading ($\zeta_b =$
498 0.3 , $\zeta_c = 0$), asymmetric sand densification is predicted on the
499 opposite sides of the pile. In the case of dense sand, some
500 net sand loosening is also visible along the upper shaft (on

the back-side with respect to the loading direction), due to
compression relief and shear-induced dilation.

501
502
503 The final D_r distributions in Fig. 7 are an outcome of the
504 local response history at soil element. Relevant features of
505 such a response are illustrated in Figs. 8-11, particularly for
506 the reference elements (A, B, C, D) indicated in Fig. 2 and
507 the simulations cases L2 ($D_r = 30\%$) and D2 ($D_r = 70\%$).
508 Fig. 8 shows cyclic strain paths in terms of deviatoric and
509 volumetric strain invariants, with the colour sidebars indicating
510 the number of cycles gradually elapsed. The intensity of soil
511 straining depends on the specific location of each reference
512 element, and it was expected that shallow elements on the front-
513 side of the pile (i.e., within the ‘passive’ soil mass) would
514 experience overall larger deformation with a more pronounced
515 volumetric component – note that the strain paths at elements
516 A-B (Figs. 8a-8b) are steeper than at elements C-D (Figs. 8c-
517 8d). The timing of soil straining along the cyclic history appears
518 to depend both on the soil location and the initial relative
519 density. For instance, the dependence on D_r is particularly
520 evident for elements A and C (Fig. 8a): in the case of $D_r =$
521 30% , the soil deforms mostly during the first 30 cycles, so
522 that the response to the remaining 70 cycles develops at nearly
523 constant volume. The ratcheting response of the soil is directly
524 related in SANISAND-MS to the evolution of the memory
525 locus, particularly of its size m^M (Fig. 1). Fig. 9 confirms
526 the close correlation between the strain paths in Fig. 8 and
527 the evolution of m^M against the number of cycles. The rate
528 of m^M variations reflects how quickly the soil approaches a
529 state of larger stiffness and slower strain accumulation, which
530 is phenomenologically represented by an expanded memory
531 surface (Liu *et al.*, 2019b). ‘Irregular’ $m^M - N$ trends such
532 as those simulated for element A are indicative of alternating
533 expansion and contraction of the memory surface, with the
534 latter being triggered by volumetric dilation according to Eq.
535 (3). Generally, the memory surface is more likely to exhibit
536 such a behaviour at shallow soil locations, i.e., where the mean
537 effective stress is low and dilation more easily triggered.

538 The stress paths simulated at the same reference points are
539 displayed in Fig. 10 in terms of mean effective stress (p) and
540 deviatoric stress invariant (q) – for brevity, only for the case
541 of $D_r = 70\%$. As observed for their strain counterparts, also
542 stress paths evolve during cycling at a rate depending on several
543 governing factors. It seems interesting to observe that, while
544 strain paths may cyclically evolve towards (nearly) isochoric
545 conditions (Fig. 8), a gradual decrease in p takes place, up
546 to the attainment of ‘undrained-like’ $q - p$ response loops –
547 see, e.g., elements B-C. Fig. 11 reveals the extent of such a
548 phenomenon by showing the distribution of the p/p_{in} ratio
549 between the final ($N = 100$, at minimum/nil lateral load) and
550 the initial (after gravity loading) values of mean effective stress.
551 Both in loose and dense sand, an extended mass of soil around
552 the pile reaches p/p_{in} values lower than 1, particularly where
553 severe shear loading occurs. Repeated shear loading causes
554 a gradual densification of the soil, which is accompanied by

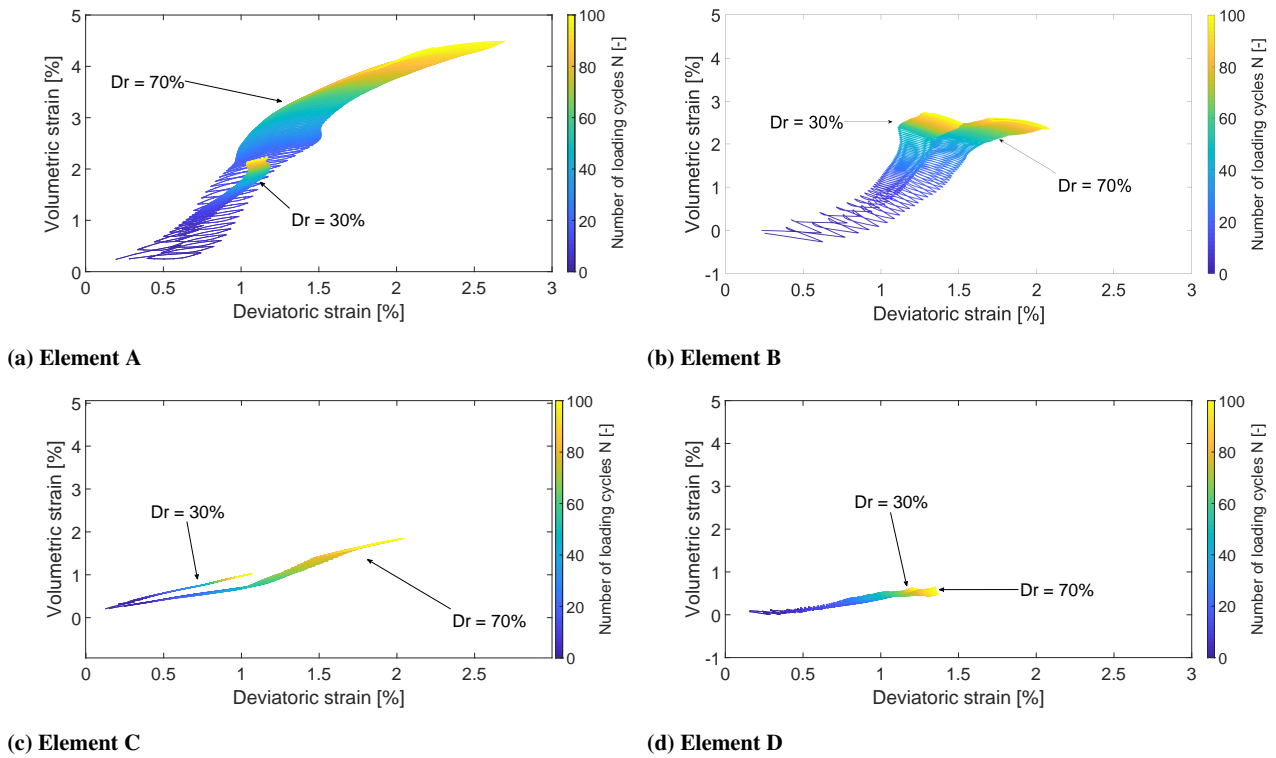


Fig. 8. Cyclic strain paths at the reference elements in Fig. 2. Values of volumetric and deviatoric strain invariants were obtained from the total (ε_{ij}) and deviatoric (e_{ij}) strain tensors as ε_{kk} and $\sqrt{(2/3)e_{ij}e_{ij}}$, respectively. Simulation cases L2 and D2.

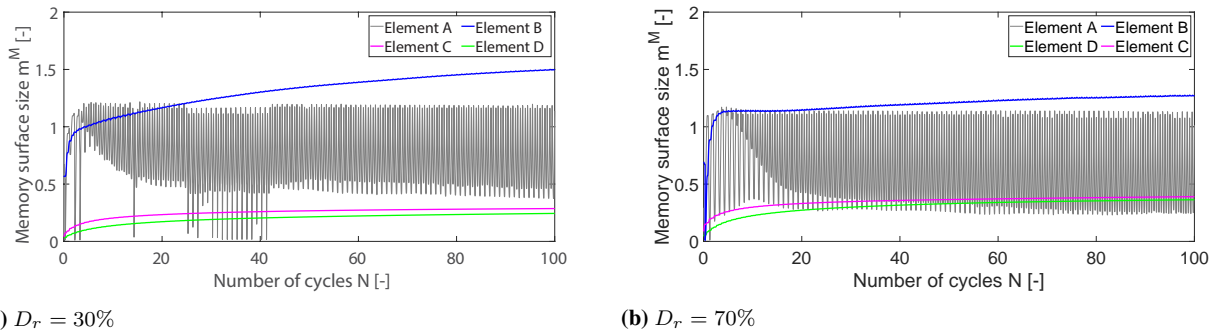


Fig. 9. Evolution of the memory surface size at the reference elements in Fig. 2 – simulation cases (a) L2 and (b) D2.

555 the observed reduction in mean stress due to the continuity of
 556 contiguous soil elements around the pile. The same kind of
 557 interaction between cyclic loading and kinematic constraints, as
 558 well as similar undrained-like stress paths, have been recorded
 559 experimentally by *Tsuha et al. (2012)* during small-scale tests
 560 on piles subjected to axial cyclic loading. The final achievement
 561 of a certain p/p_{in} distribution are clearly a function of the
 562 specific soil behaviour, as well as of the magnitude, asymmetry,
 563 and duration of the enforced cyclic loading.

564 Although more complex than in element test analyses, the
 565 simulated soil response around a monopile complies well with
 566 the intended performance of the SANISAND-MS model (*Liu*
 567 *et al., 2019b, 2020*). Nonetheless, a note should be made about
 568 the calibration of sand's parameters in relation to monopile
 569 applications. While 3D FE results suggest that significant strain
 570 accumulation occurs at shallow soil locations, the reference

SANISAND-MS parameters in Table 2 were identified against 571
 high-cyclic triaxial test results obtained under relatively large 572
 mean effective stress – equal to 100–200 kPa in most cases. This 573
 aspect should be carefully considered in the planning of future 574
 high-cyclic testing programmes, so as to enable more accurate 575
 modelling of cyclic behaviour at low confinement. 576

COMPARISON TO MONOPILE TILT DATA

In this section the tilting of the monopile returned by 577
 SANISAND-MS 3D FE analyses is discussed in more 578
 detail in comparison to existing experimental evidence. 579
 Given the limited number of simulated cycles ($N = 100$), 580
 however, the numerical results in hand do not directly relate 581
 to the long-term loading experienced by real monopiles 582
 in the field. Nonetheless, such a limitation should not 583
 devalue a modelling framework that supports in-depth 584

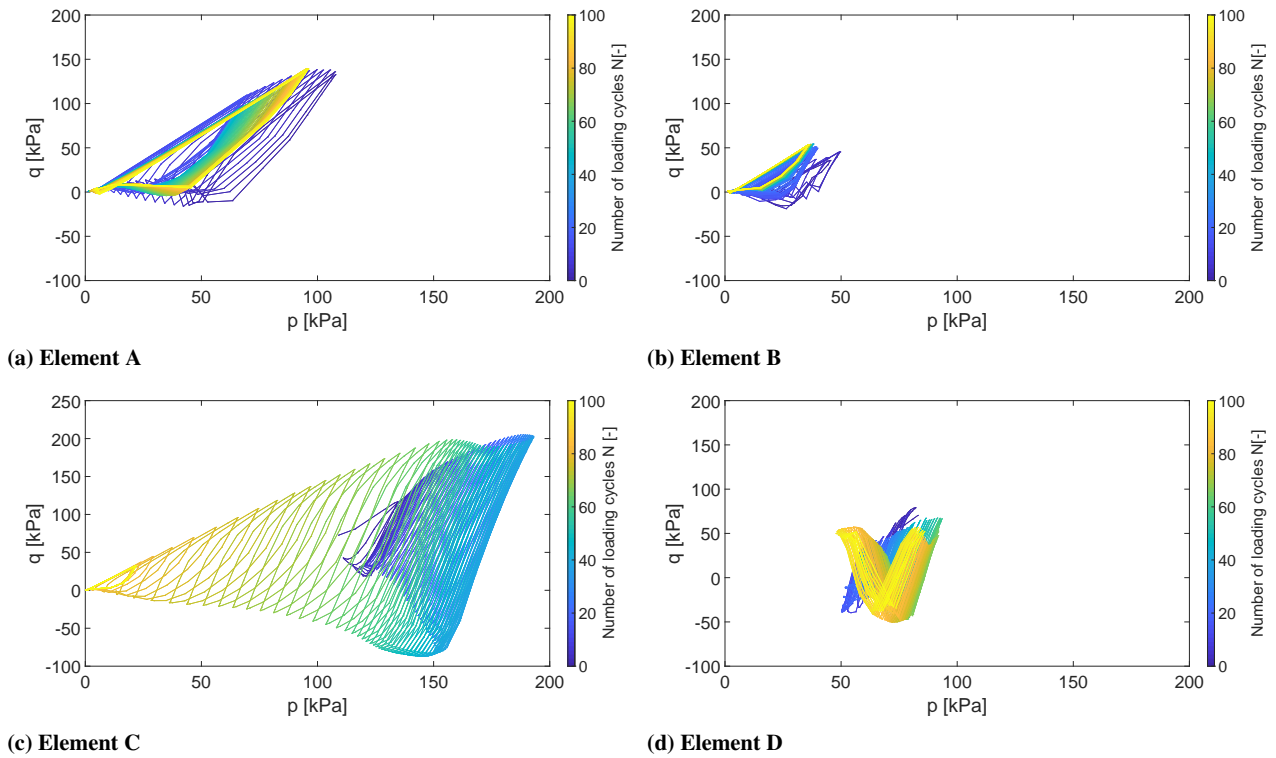


Fig. 10. Cyclic effective stress paths at the reference elements in Fig. 2. Values of mean and deviatoric stress invariants were obtained from the effective stress tensor (σ_{ij}) and deviatoric (s_{ij}) effective stress tensors as $\sigma_{kk}/3$ and $\sqrt{(3/2)s_{ij}s_{ij}} \cdot \cos(3\theta_\sigma)$, respectively, where θ_σ stands for the Lode angle. Simulation case D2.

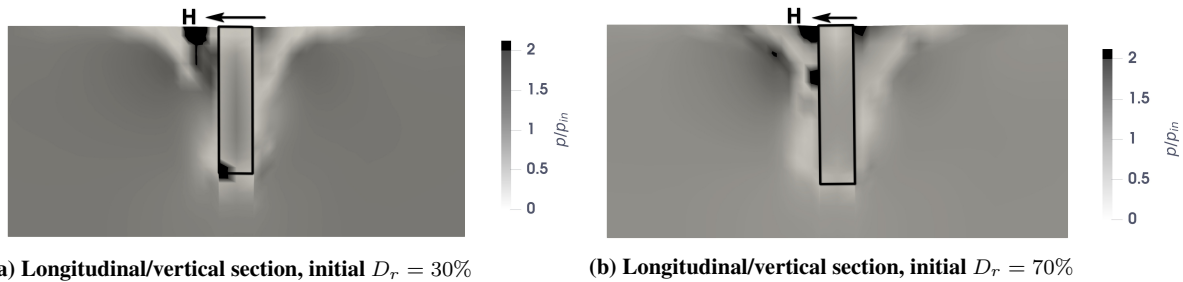


Fig. 11. Distribution of the p/p_{in} ratio between the final ($N = 100$, nil lateral load) and the initial (after gravity loading) values of mean effective stress – simulation cases (a) L2 and (b) D2.

585 understanding of geotechnical mechanisms (see previous
586 section) and, potentially, a mechanics-based refinement of
587 design approaches.

588 Experimental and numerical results regarding monopile tilt
589 are compared in Fig. 12 in relation to pure one-way cyclic
590 loading ($\zeta_c = 0$) of different amplitude ratio ζ_b (Eq. (5)) –
591 3D FE tilt trends were plotted by selecting, for each cycle,
592 monopile rotation values associated with the maximum load
593 amplitude. 1g small-scale experimental results from Richards
594 *et al.* (2019) (Fig. 12a – $D_r = 1\%$, and Fig. 12b – $D_r = 60\%$)
595 and LeBlanc *et al.* (2010) (Fig. 12c – $D_r = 4\%$, and Fig. 12d
596 – $D_r = 38\%$) were selected for semi-quantitative comparison.
597 A well-known point of attention about 1g physical modelling
598 regards the scaling of sand's dilatancy, which is inherently
599 stress-dependent (Bolton, 1986): the behaviour of a prototype
600 pile in medium-dense/dense sand is best reproduced in 1g
601 scaled tests using a lower relative density, given the larger

dilatancy that sand exhibits at low stress levels. The interested
reader is referred to LeBlanc *et al.* (2010) and Richards *et al.*
(2019) for further discussion of geotechnical scaling in pile-
sand models. The tests selected from LeBlanc *et al.*'s and
Richards *et al.*'s database were deemed representative of soil
conditions broadly comparable to those assumed in the (full-
scale) FE model – i.e., to a monopile in loose and dense sand.
Out of the simulation programme in Table 3, the 3D FE results
obtained for the cases L1–L3 and D1–D3 are illustrated in Figs.
12e ($D_r = 30\%$) and 12f ($D_r = 70\%$).

Both experimental and simulation results indicate that, under
pure one-way cyclic loading, higher ζ_b values lead to the
accumulation of larger pile rotation. Quantitatively, 3D FE
simulations returned $\Delta\theta/\theta_s$ values in the order of 10^0 after 100
cycles. Such values are consistent with the experimental data
reported by LeBlanc *et al.* (2010), who obtained normalised
rotation values of about $7 \sim 8 \times 10^{-1}$ under similar cyclic

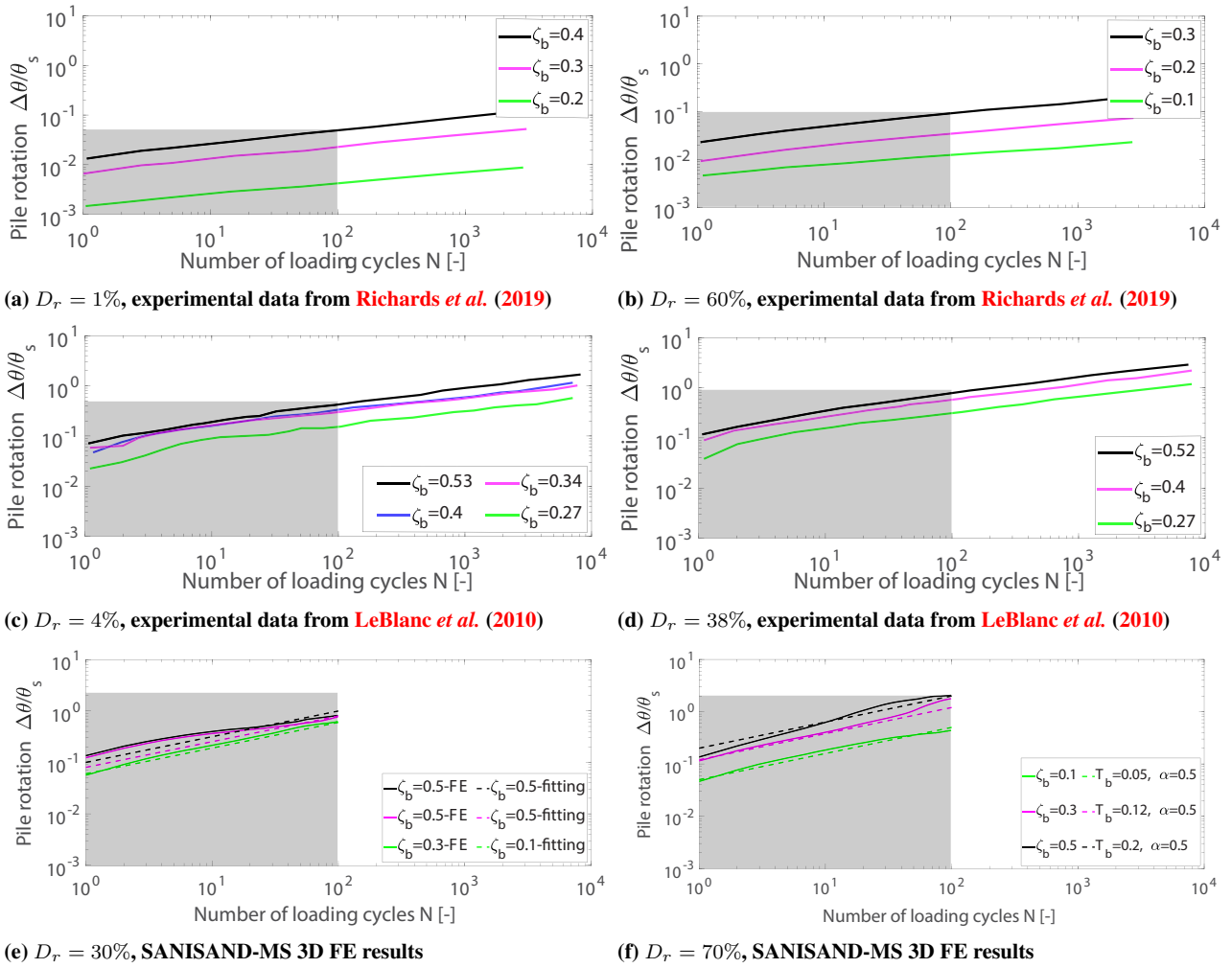


Fig. 12. Influence of the cyclic load amplitude ratio (ζ_b) on the normalised pile rotation ($\Delta\theta/\theta_s$) against the number of loading cycles (N). Both Experimental and 3D FE results correspond with pure one-way cyclic loading ($\zeta_c = 0$).

619 loading conditions. In contrast, Richards *et al.*'s data show
 620 after 100 cycles smaller $\Delta\theta/\theta_s - N$ values. In this respect, it
 621 should also be recalled that SANISAND-MS parameters were
 622 originally calibrated to achieve best agreement with soil test
 623 data over 10^4 cycles (Wichtmann, 2005; Liu *et al.*, 2019b). In
 624 fact, quantitatively different FE results could be obtained after
 625 alternative calibration choices.

626 Fig. 13 displays the influence of a positive asymmetry ratio
 627 ζ_c on monopile tilting under biased one-way cyclic loading
 628 (i.e., with no change in the sign of the load), for the case of $\zeta_b =$
 629 0.3. SANISAND-MS 3D FE results (Fig. 13c – $D_r = 30\%$, and
 630 Fig. 13d – and 70% ; simulations L7, L8, L9 and D7, D8, D9 in
 631 Table 3) and experimental data from LeBlanc *et al.* (2010) (Fig.
 632 13a – $D_r = 4\%$, and Fig. 13b – $D_r = 38\%$) are compared in the
 633 figure, and support altogether the following conclusions:

- 634 1. nearly linear tilt accumulation trends in bi-logarithmic
 635 plots;
- 636 2. the accumulated rotation after 100 cycles lies in the
 637 $10^{-1} - 10^0$ range;
- 638 3. a lower accumulated rotation is obtained at increasing ζ_c
 639 when $\zeta_c \geq 0$.

640 3D FE and experimental results could be further compared
 641 as in Figs. 12-13 for cases of two-way cyclic loading (i.e.,
 642 with negative ζ_c – simulations cases L10, L11, L12 and D10,
 643 D11, D12 in Table 3). However, it was preferred to prioritise
 644 in the following a broader assessment of 3D FE results against
 645 existing simplified approaches for monopile tilt calculations. In
 646 particular, recent experimental studies have supported the use
 647 of the following empirical relationship (LeBlanc *et al.*, 2010):

$$\frac{\Delta\theta}{\theta_s} = T_b(\zeta_b) T_c(\zeta_c) N^\alpha \quad (6)$$

648 which enables straightforward quantification of the normalised
 649 monopile rotation under single-amplitude, unidirectional cyclic
 650 loading. In Eq. (6) T_b and T_c are dimensionless functions
 651 separately accounting for the influence of ζ_b and ζ_c ,
 652 respectively, while α is a ratcheting exponent; in particular,
 653 the definition of T_c is such that $T_c(\zeta_c = 0) = 1$ and $T_c(\zeta_c =$
 654 $1) = 0$. LeBlanc *et al.* (2010) recognised that T_b increases
 655 linearly with ζ_b depending on the relative density, whereas T_c
 656 was found to be a D_r -insensitive, non-monotonic function of
 657 ζ_c ; the same authors proposed for their dataset a single value
 658 of the ratcheting exponent, $\alpha = 0.31$, unaffected by D_r , ζ_b ,
 659

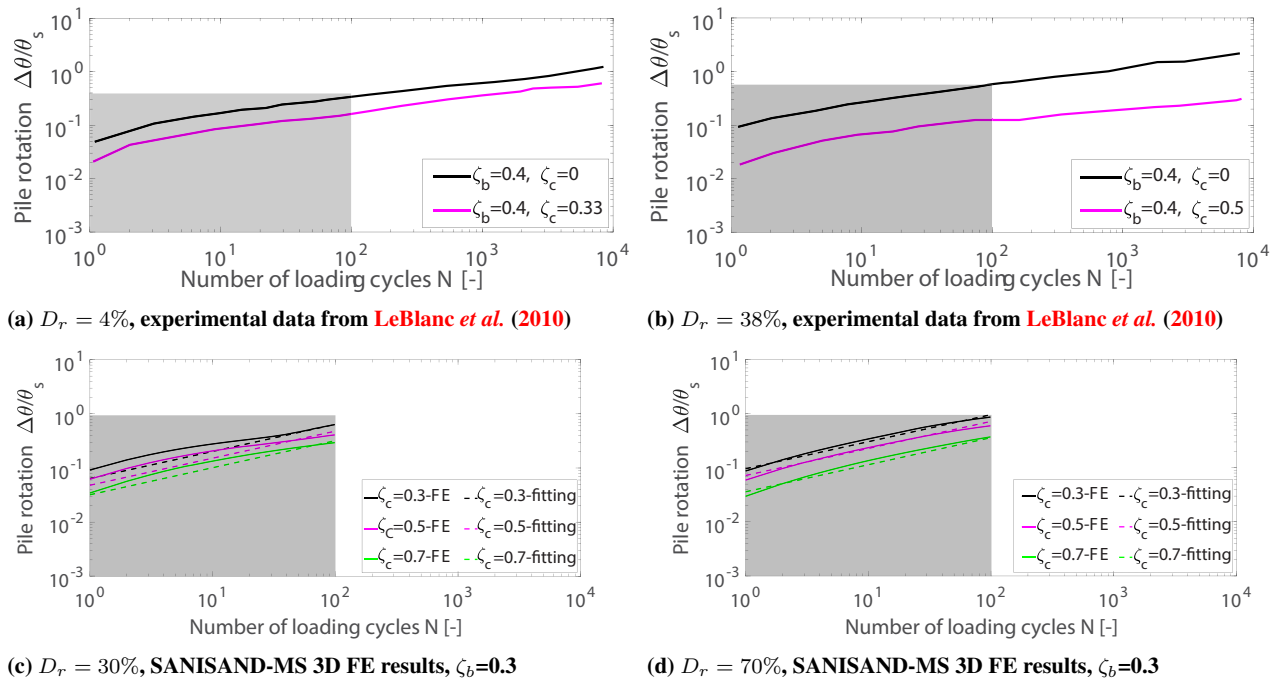


Fig. 13. Influence of a positive cyclic load asymmetry ratio (ζ_c) on the normalised pile rotation ($\Delta\theta/\theta_s$) against the number of loading cycles (N).

659 and ζ_c – which differs, however, from the conclusions that
 660 **Truong *et al.* (2019)** drew based on centrifuge test results. As
 661 reported in Table 3, T_b - T_c values were also estimated in this
 662 study for all FE simulation cases via ‘visual’ curve fitting of
 663 numerical rotation trends. For simplicity, a single value of the
 664 ratcheting exponent equal to $\alpha = 0.5$ was identified, although
 665 more accurate fitting could be obtained through ζ_c -dependent
 666 α values (**Truong *et al.*, 2019; Richards *et al.*, 2019**).

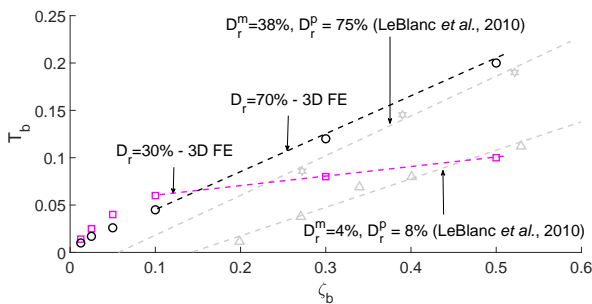


Fig. 14. Comparison between experimental (1g) and numerical $T_b - \zeta_b$ trends for loose and dense sand – pure one one-way cyclic loading ($\zeta_c = 0$). Relative density values for the reference test data are provided for model (D_r^m) and prototype (D_r^p) scales as per **LeBlanc *et al.* (2010)**.

667 The $T_b - \zeta_b$ trends inferred from SANISAND-MS 3D FE
 668 results are reported in Fig. 14 alongside those from **LeBlanc
 669 *et al.* (2010)**. The reference experimental data suggest that the
 670 slope of the $T_b - \zeta_b$ trends increases with the relative density
 671 of the sand. The numerical results in Fig. 14 support similar
 672 conclusions for ζ_b values larger than 0.1, whereas they deviate
 673 from linearity at low amplitude ratios – most apparently for the
 674 case of loose sand. Such a non-linearity is compatible with the

intuitive fact that no monopile tilt should occur under vanishing
 675 cyclic load amplitude. However, existing experimental data do
 676 not inform sufficiently about monopile tilt at $\zeta_b < 0.1$, so that
 677 more extensive studies, both experimental and numerical, will
 678 be necessary to clarify this aspect.
 679

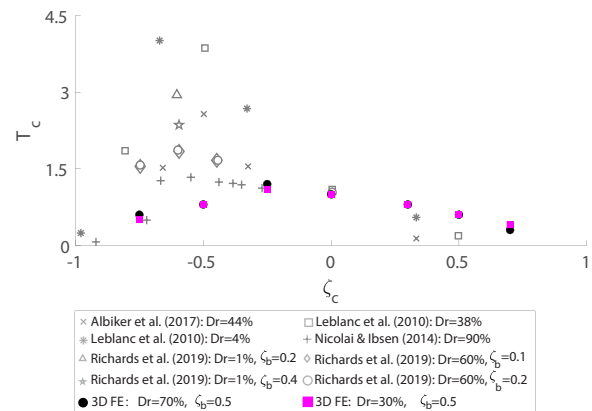


Fig. 15. Comparison between experimental (1g) and numerical $T_c - \zeta_c$ trends for loose and dense sand.

Similarly, Fig. 15 presents a comparison between numerical
 680 $T_c - \zeta_c$ trends and those associated with selected experimental
 681 datasets – namely, from **LeBlanc *et al.* (2010); Nicolai &
 682 Ibsen (2014); Albiker *et al.* (2017); Richards *et al.* (2019)**.
 683 In agreement with **LeBlanc *et al.* (2010)**’s observations,
 684 the T_c values emerging from numerical simulations are
 685 markedly insensitive to D_r . While the simulated $T_c - \zeta_c$ trend
 686 agrees qualitatively with all reference data, some quantitative
 687 differences are apparent, for instance in terms of maximum T_c
 688 and associated value of ζ_c . Such differences may be attributed
 689

690 to different experimental settings, sand characteristics and
 691 scaling effects, and will require further studies to be deciphered.
 692 For instance, the quantitative impact of different gravity
 693 levels in small-scale testing has been recently pointed out by
 694 Richards (2019). Overall, Figs. 14-15 confirm that the proposed
 695 SANISAND-MS 3D FE framework can produce results in
 696 general agreement with experimental evidence, at least within
 697 the limited number of loading cycles considered in this study.
 698 As shown throughout this work, implicit 3D FE modelling has
 699 potential to enhance the detailed interpretation of monopile-soil
 700 interaction mechanisms, and enable parametric studies more
 701 extensive than feasible through testing.

CONCLUDING REMARKS

702 In this study, implicit 3D FE modelling was combined with the
 703 memory-enhanced, bounding surface SANISAND-MS model
 704 to numerically analyse monopile behaviour under lateral cyclic
 705 loading in dry sand. The selection of SANISAND-MS was
 706 motivated by its proven ability to reproduce cyclic ratcheting
 707 in sand samples. Parametric studies were carried out to
 708 numerically investigate the link between local soil behaviour
 709 and global monopile response to cyclic loading – particularly
 710 its lateral tilt. The significant computational costs of implicit 3D
 711 FE modelling imposed to limit the numerical study to relatively
 712 short loading histories (100 cycles), with obvious impact on
 713 the possibility to extend numerical observations to real field
 714 conditions.

715 Semi-quantitative comparison to experimental data from the
 716 literature supported the suitability of the proposed modelling
 717 approach. In particular, it was possible to confirm typical
 718 assumptions usually associated with empirical tilt prediction
 719 methods, mostly regarding the relationship between tilting
 720 trends and magnitude/asymmetry of (single-amplitude) cyclic
 721 loading.

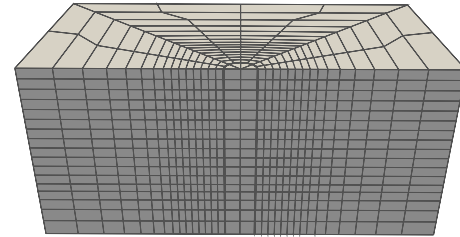
722 Even when limited to short-term cyclic loading, implicit 3D
 723 FE modelling can shed light on the geotechnical mechanisms
 724 underlying relevant response features at the foundation level.
 725 Importantly, detailed 3D modelling of monopile-soil interaction
 726 can help to evaluate the implications of different design choices
 727 and/or soil parameters uncertainly estimated. Such possibilities
 728 may positively impact the soundness of offshore geotechnical
 729 practice, and are not equally enabled by simpler 0D/1D
 730 modelling approaches.

731 Future work along this research line will continue to
 732 explore the role of relevant governing factors, such as, e.g.,
 733 pile slenderness, eccentricity and orientation of the lateral
 734 load, pore pressure effects in water-saturated soil. The results
 735 presented in this paper encourage more intensive use of implicit
 736 SANISAND-MS 3D FE modelling, particularly to inspire
 737 enhanced design methods for cyclically loaded foundations –
 738 not limited to offshore monopiles.

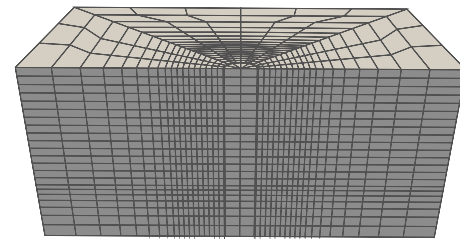
APPENDIX – ACCURACY OF 3D FE RESULTS

Mesh sensitivity

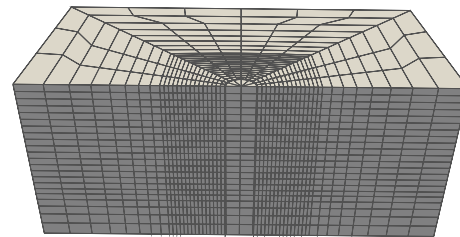
739



(a) 2399 elements



(b) 5571 elements



(c) 6755 elements

Fig. 16. Auxiliary 3D FE models adopted for the mesh sensitivity study.

740 The size of the soil domain in Fig. 2 was determined to prevent
 741 boundary effects, in agreement with previous indications
 742 from Corciulo *et al.* (2017). Afterwards, the sensitivity of FE
 743 results to space discretization was investigated. To this end,
 744 the FE results obtained using the four meshes in Fig. 2 and
 745 Fig. 16 were compared for the simulation case L6 in Table 3
 746 – total number of SSP elements equal to 2399, 4181, 5571,
 747 6755 in Figs. 16a, 2, 16b, 16c, respectively. Fig. 17 displays
 748 the pile responses associated with the four meshes, in terms
 749 of force-displacement cycles (Fig. 17a) and accumulated pile
 750 displacement against the number of cycles (Fig. 17b). Finer
 751 meshes appear to result in larger accumulated displacement. As
 752 a converging trend was clearly observed upon mesh refinement,
 753 the mesh in Fig. 2 (4181 elements) was finally selected as a
 754 trade-off between accuracy and efficiency. It is worth mention-
 755 ing that the calculation time for (sequential) 3D FE simulations
 756 ranged, for 100 loading cycles, from 16 hours (coarsest mesh)
 757 to 82 hours (finest mesh), and was about 49 hours for the
 758 selected mesh in Fig. 2.

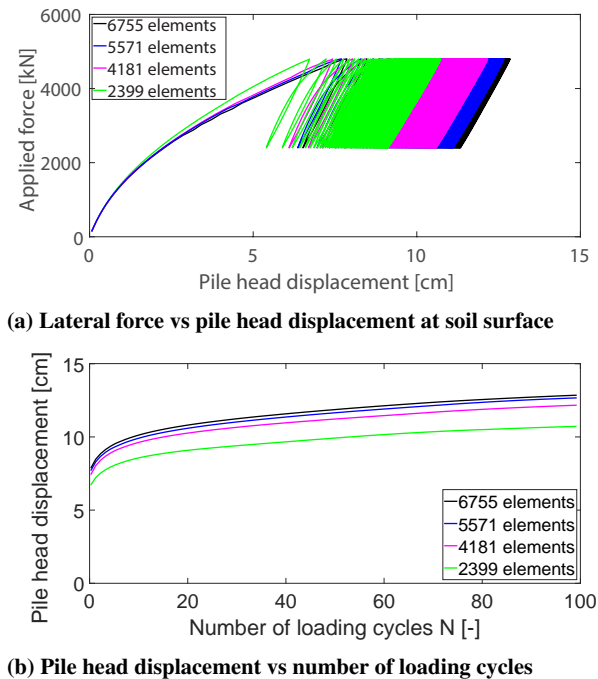


Fig. 17. Mesh sensitivity effects in the monopile response to lateral cyclic loading ($D_r = 30\%$, simulation case L6 in Table 3).

759 Influence of stress-point integration settings

760 Stress integration at individual Gauss points (one per SSP
761 element) was performed using an explicit Runge-Kutta (RK)
762 algorithm of the type described in Sloan *et al.* (2001). In
763 the authors' experience, explicit integration is well suited for
764 cyclic/dynamic loading conditions, i.e., in the presence of
765 frequent stress reversals. From an implementation standpoint,
766 the adopted RK algorithm:

- 767 – features fourth-order accuracy, as in the version
768 described by Sloan (1987);
- 769 – operates automatic sub-stepping based on an estimate of
770 the integration error obtained by comparing fourth- and
771 fifth-order RK solutions. Sub-stepping is performed until
772 the estimated (normalised) error is found to be better
773 than an input tolerance $STOL$;
- 774 – recognises the local transition from elastic to elasto-
775 plastic response when the computed yield function is
776 larger than $FTOL$.

777 All the numerical results presented in this work were
778 obtained after setting $STOL = 10^{-4}$ and $FTOL = 10^{-4}$ kPa.
779 Obviously, lower values of $STOL$ and $FTOL$ would be in
780 favour of higher accuracy, though with increased computational
781 burden. Stress integration with error-driven sub-stepping was
782 deemed particularly appropriate for the application in hand, as
783 unreliable FE results would be obtained if numerical errors
784 were left free to accumulate. In contrast, the inclusion of
785 automatic sub-stepping allowed a desired level of accuracy
786 to be preserved across the soil domain, also at shallow soil
787 locations where accurate stress integration is notoriously more
788 difficult.

789 Figs. 18-19 illustrate the impact of RK integration settings
790 on the stress response simulated at elements B (shallow) and D
791 (deeper) in Fig. 2. In particular, the mean effective stress (p)
792 and the deviatoric stress invariant (q) are plotted against the
793 number of calculation steps for the simulation case L2 in Table
794 3. To analyse the effects of different RK integration settings,
795 cyclic strain histories were extracted from the reference FE
796 solution at the selected elements, and then re-applied in the
797 RK integration routine to re-calculate stresses for different
798 values of $STOL$ (Fig. 18) and $FTOL$ (Fig. 19). While it is
799 acknowledged that the extracted strain histories would also
800 be affected by the mentioned integration settings, the adopted
801 approach was considered a simpler, yet informative, way to
802 perform the intended analysis. Overall, Figs. 18-19 support
803 the validity of the selected integration settings, as they show
804 that 'harsher' choices would have not produced appreciably
805 different results – not even at shallow soil locations.

ACKNOWLEDGEMENTS

806 The authors wish to acknowledge the China Scholarship
807 Council (CSC) and the Geo-Engineering Section of Delft
808 University of Technology for financial support of the first
809 author. The detailed and constructive feedback of two
810 anonymous reviewers is also greatly appreciated.

REFERENCES

- 812 Abadie, C. N., Byrne, B. W. & Houlsby, G. T. (2019a). Rigid pile
813 response to cyclic lateral loading: laboratory tests. *Géotechnique*
814 **69**, No. 10, 863–876.
- 815 Abadie, C. N., Houlsby, G. & Byrne, B. (2019b). A method
816 for calibration of the hyperplastic accelerated ratcheting model
817 (HARM). *Computers and Geotechnics* **112**, 370–385.
- 818 Achmus, M., Kuo, Y.-S. & Abdel-Rahman, K. (2009). Behavior of
819 monopile foundations under cyclic lateral load. *Computers and*
820 *Geotechnics* **36**, No. 5, 725–735.
- 821 Achmus, M., Schmoor, K. A., Herwig, V. & Matlock, B. (2020).
822 Lateral bearing behaviour of vibro-and impact-driven large-
823 diameter piles in dense sand. *geotechnik* **43**, No. 3, 147–159.
- 824 Albiker, J., Achmus, M., Frick, D. & Flindt, F. (2017). 1 g model tests
825 on the displacement accumulation of large-diameter piles under
826 cyclic lateral loading. *Geotechnical Testing Journal* **40**, No. 2, 173–
827 184.
- 828 Anusic, I., Lehane, B., Eiksund, G. & Liingaard, M. (2019). Influence
829 of installation method on static lateral response of displacement
830 piles in sand. *Géotechnique Letters* **9**, No. 3, 193–197.
- 831 Arany, L., Bhattacharya, S., Macdonald, J. H., Hogan, S. J. *et al.*
832 (2015). A critical review of serviceability limit state requirements
833 for monopile foundations of offshore wind turbines. In *Offshore*
834 *Technology Conference*, Offshore Technology Conference.
- 835 Archer, C., Simão, H., Kempton, W., Powell, W. & Dvorak, M. (2017).
836 The challenge of integrating offshore wind power in the US electric
837 grid. part I: Wind forecast error. *Renewable energy* **103**, 346–360.
- 838 Barari, A., Bagheri, M., Rouainia, M. & Ibsen, L. B. (2017).
839 Deformation mechanisms for offshore monopile foundations

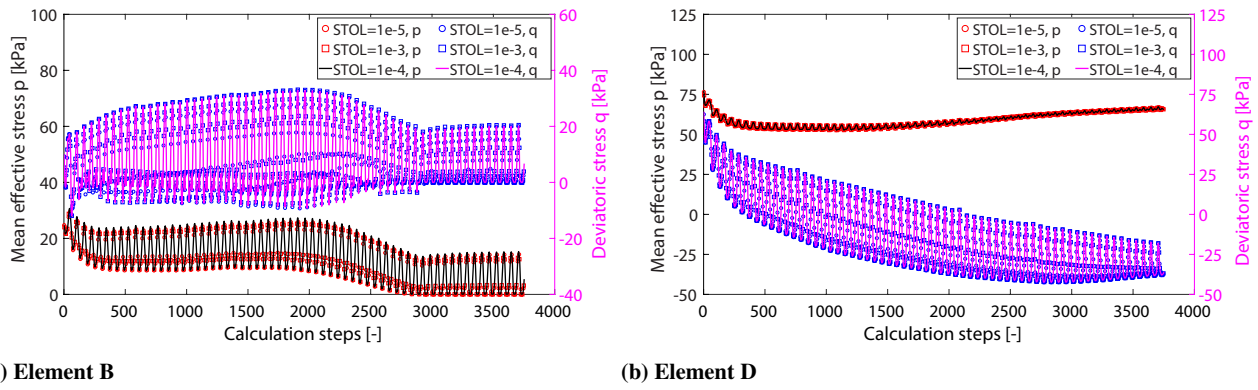


Fig. 18. Influence of $STOL$ (tolerance for error-driven sub-stepping) on stress integration at elements B and D in Fig. 2 – simulation case L2 in Table 3. Values of mean and deviatoric stress invariants were obtained from the total (σ_{ij}) and deviatoric (s_{ij}) effective stress tensors as $\sigma_{kk}/3$ and $\sqrt{(3/2)s_{ij}s_{ij}} \cdot \cos(3\theta_\sigma)$, respectively, where θ_σ stands for the Lode angle.

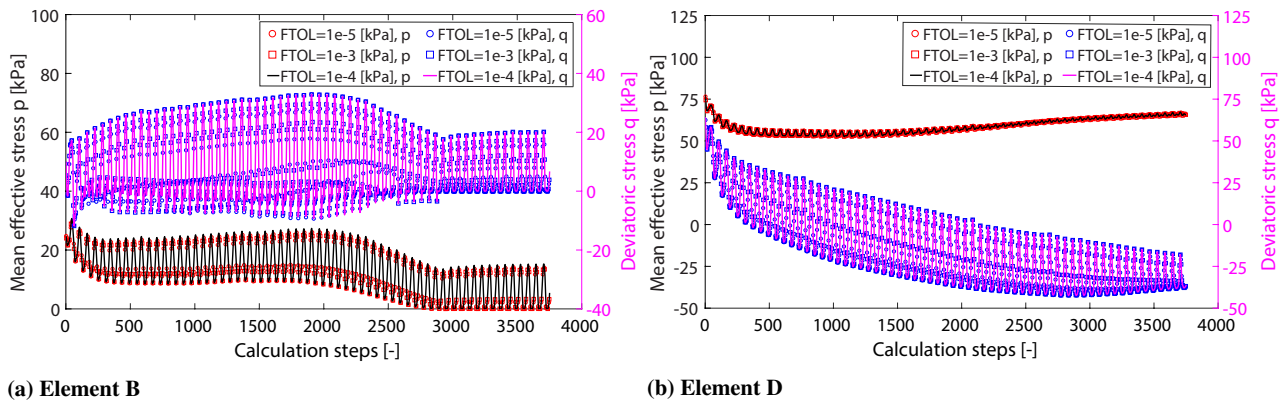


Fig. 19. Influence of $FTOL$ (tolerance for the yielding test) on stress integration at elements B and D in Fig. 2 – simulation case L2 in Table 3. Values of mean and deviatoric stress invariants were obtained from the total (σ_{ij}) and deviatoric (s_{ij}) effective stress tensors as $\sigma_{kk}/3$ and $\sqrt{(3/2)s_{ij}s_{ij}} \cdot \cos(3\theta_\sigma)$, respectively, where θ_σ stands for the Lode angle.

840 accounting for cyclic mobility effects. *Soil Dynamics and*
 841 *Earthquake Engineering* **97**, 439–453.
 842 Been, K. & Jefferies, M. G. (1985). A state parameter for sands.
 843 *Géotechnique* **35**, No. 2, 99–112.
 844 Bhattacharya, S. (2019). *Design of foundations for offshore wind*
 845 *turbines*. Wiley Online Library.
 846 Bolton, M. (1986). Strength and dilatancy of sands. *Geotechnique* **36**,
 847 No. 1, 65–78.
 848 Borja, R. I. & Amies, A. P. (1994). Multiaxial cyclic plasticity model
 849 for clays. *Journal of geotechnical engineering* **120**, No. 6, 1051–
 850 1070.
 851 Cerfontaine, B., Dieudonné, A.-C., Radu, J.-P., Collin, F. & Charlier,
 852 R. (2015). 3D zero-thickness coupled interface finite element:
 853 Formulation and application. *Computers and Geotechnics* **69**, 124–
 854 140.
 855 Chancham, C., Waewsak, J. & Gagnon, Y. (2017). Offshore wind
 856 resource assessment and wind power plant optimization in the gulf
 857 of thailand. *Energy* **139**, 706–731.
 858 Cheng, X., Diambra, A., Ibraim, E., Liu, H. Y. & Pisanò, F. (2021). 3D
 859 FE-informed laboratory soil testing for the design of offshore wind
 860 turbine monopiles. *Journal of Marine Science and Engineering*,
 861 accepted for publication.
 862 Chong, S.-H. (2017). Numerical simulation of offshore foundations
 863 subjected to repetitive loads. *Ocean Engineering* **142**, 470–477.

Corciulo, S., Zanolì, O. & Pisanò, F. (2017). Transient response of
 864 offshore wind turbines on monopiles in sand: role of cyclic hydro-
 865 mechanical soil behaviour. *Computers and Geotechnics* **83**, 221–
 866 238.
 867
 868 Corti, R., Diambra, A., Muir Wood, D., Escribano, D. E. & Nash, D. F.
 869 (2016). Memory surface hardening model for granular soils under
 870 repeated loading conditions. *Journal of Engineering Mechanics*,
 871 04016102.
 872 Cuéllar, P., Baeßler, M. & Rücker, W. (2009). Ratcheting convective
 873 cells of sand grains around offshore piles under cyclic lateral loads.
 874 *Granular Matter* **11**, No. 6, 379.
 875 Cuéllar, P., Mira, P., Pastor, M., Merodo, J. A. F., Baeßler, M. &
 876 Rücker, W. (2014). A numerical model for the transient analysis
 877 of offshore foundations under cyclic loading. *Computers and*
 878 *Geotechnics* **59**, 75–86.
 879 Dafalias, Y. F. & Manzari, M. T. (2004). Simple plasticity sand
 880 model accounting for fabric change effects. *Journal of Engineering*
 881 *mechanics* **130**, No. 6, 622–634.
 882 Day, R. & Potts, D. (1994). Zero thickness interface elements numerical
 883 stability and application. *International Journal for numerical and*
 884 *analytical methods in geomechanics* **18**, No. 10, 689–708.
 885 di Prisco, C. & Mortara, G. (2013). A multi-mechanism constitutive
 886 model for plastic adaption under cyclic loading. *International*
 887 *Journal for Numerical and Analytical Methods in Geomechanics*
 888 **37**, No. 18, 3071–3086.

- 889 di Prisco, C. & Pisanò, F. (2011). Seismic response of rigid
890 shallow footings. *European Journal of Environmental and Civil*
891 *Engineering* **15**, No. sup1, 185–221.
- 892 Gao, G. & Meguid, M. (2018). Effect of particle shape on the response
893 of geogrid-reinforced systems: insights from 3D discrete element
894 analysis. *Geotextiles and Geomembranes* **46**, No. 6, 685–698.
- 895 Ghofrani, A. & Arduino, P. (2018). Prediction of leap centrifuge test
896 results using a pressure-dependent bounding surface constitutive
897 model. *Soil Dynamics and Earthquake Engineering* **113**, 758–770.
- 898 Griffiths, D. (1985). Numerical modelling of interfaces using
899 conventional finite elements. In *International conference on*
900 *numerical methods in geomechanics*, pp. 837–844.
- 901 Heins, E., Bienen, B., Randolph, M. F. & Grabe, J. (2020). Effect
902 of installation method on static and dynamic load test response
903 for piles in sand. *International Journal of Physical Modelling in*
904 *Geotechnics* **20**, No. 1, 1–23.
- 905 Houlsby, G. (2016). Interactions in offshore foundation design.
906 *Géotechnique* **66**, No. 10.
- 907 Houlsby, G., Abadie, C., Beuckelaers, W. & Byrne, B. (2017). A model
908 for nonlinear hysteretic and ratcheting behaviour. *International*
909 *Journal of Solids and Structures* **120**, 67–80.
- 910 Jostad, H., Grimstad, G., Andersen, K., Saue, M., Shin, Y. & You,
911 D. (2014). A FE procedure for foundation design of offshore
912 structures—applied to study a potential owt monopile foundation in
913 the korean western sea. *Geotechnical Engineering Journal of the*
914 *SEAGS & AGSSEA* **45**, No. 4, 63–72.
- 915 Jostad, H. P., Dahl, B. M., Page, A., Sivasithamparam, N. & Sturm, H.
916 (2020). Evaluation of soil models for improved design of offshore
917 wind turbine foundations in dense sand. *Géotechnique*, 1–18.
- 918 Kementzetzidis, E., Corciulo, S., Versteijlen, W. G. & Pisanò, F.
919 (2019). Geotechnical aspects of offshore wind turbine dynamics
920 from 3d non-linear soil-structure simulations. *Soil Dynamics and*
921 *Earthquake Engineering* **120**, 181–199.
- 922 Kementzetzidis, E., Metrikine, A. V., Versteijlen, W. G. & Pisanò,
923 F. (2020). Frequency effects in the dynamic lateral stiffness of
924 monopiles in sand: insight from field tests and 3D FE modelling.
925 *Géotechnique*, Ahead of print.
- 926 Kementzetzidis, E., Versteijlen, W. G., Nernheim, A. & Pisanò, F.
927 (2018). 3d fe dynamic modelling of offshore wind turbines in sand:
928 natural frequency evolution in the pre-to after-storm transition. In
929 *Proceedings of the 9th european conference on numerical methods*
930 *in geotechnical engineering (NUMGE 2018), june 25-27, 2018,*
931 *porto, Portugal*, CRC Press, pp. 1477–1484.
- 932 Klinkvort, R. T. (2013). *Centrifuge modelling of drained lateral*
933 *pile-soil response: Application for offshore wind turbine support*
934 *structures*. Ph.D. thesis, Technical University of Denmark.
- 935 LeBlanc, C., Houlsby, G. T. & Byrne, B. W. (2010). Response of stiff
936 piles in sand to long-term cyclic lateral loading. *Géotechnique* **60**,
937 No. 2, 79–90.
- 938 Li, X. & Dafalias, Y. F. (2000). Dilatancy for cohesionless soils.
939 *Geotechnique* **50**, No. 4, 449–460.
- 940 Liu, H. Y. (2020). *Constitutive modelling of cyclic sand behaviour for*
941 *offshore foundations*. Ph.D. thesis, Delft University of Technology.
- 942 Liu, H. Y., Abell, J., Diambra, A. & Pisanò, F. (2019a). Capturing
943 cyclic mobility and preloading effects in sand using a memory-
944 surface hardening model. In *Proc. of 7th Int. Conf. on Earthquake*
945 *Geotechnical Engineering (7ICEGE)*, pp. 17–20.
- 946 Liu, H. Y., Abell, J. A., Diambra, A. & Pisanò, F. (2019b). Modelling
947 the cyclic ratcheting of sands through memory-enhanced bounding
surface plasticity. *Géotechnique* **69**, No. 9, 783–800. 948
- Liu, H. Y., Diambra, A., Abell, J. A. & Pisanò, F. (2020). Memory-
949 enhanced plasticity modeling of sand behavior under undrained
950 cyclic loading. *Journal of Geotechnical and Geoenvironmental*
951 *Engineering* **146**, No. 11, 04020122. 952
- Liu, H. Y. & Pisanò, F. (2019). Prediction of oedometer terminal
953 densities through a memory-enhanced cyclic model for sand.
954 *Géotechnique Letters* **9**, No. 2, 81–88, doi:10.1680/jgele.18.00187. 955
- Liu, H. Y., Zygounas, F., Diambra, A. & Pisanò, F. (2018). Enhanced
956 plasticity modelling of high-cyclic ratcheting and pore pressure
957 accumulation in sands. In *Numerical Methods in Geotechnical*
958 *Engineering IX, Volume 1: Proceedings of the 9th European*
959 *Conference on Numerical Methods in Geotechnical Engineering*
960 *(NUMGE 2018), June 25-27, 2018, Porto, Portugal*, CRC Press,
961 p. 87. 962
- Manzari, M. T. & Dafalias, Y. F. (1997). A critical state two-surface
963 plasticity model for sands. *Géotechnique* **47**, No. 2, 255–272. 964
- Mattar, C. & Borvarán, D. (2016). Offshore wind power simulation
965 by using WRF in the central coast of chile. *Renewable Energy* **94**,
966 22–31. 967
- McAdam, R. A., Byrne, B. W., Houlsby, G. T., Beuckelaers, W. J.,
968 Burd, H. J., Gavin, K. G., Igoe, D. J., Jardine, R. J., Martin, C. M.,
969 Muir Wood, A. *et al.* (2019). Monotonic laterally loaded pile testing
970 in a dense marine sand at dunkirk. *Géotechnique*, Ahead of print. 971
- McGann, C. R., Arduino, P. & Mackenzie-Helnwein, P. (2015).
972 A stabilized single-point finite element formulation for three-
973 dimensional dynamic analysis of saturated soils. *Computers and*
974 *Geotechnics* **66**, 126–141. 975
- McKenna, F. (2011). Opensees: a framework for earthquake
976 engineering simulation. *Computing in Science & Engineering* **13**,
977 No. 4, 58–66. 978
- Metrikine, A., Tsouvalas, A., Segeren, M., Elkadi, A., Tehrani, F.,
979 Gómez, S., Atkinson, R., Pisanò, F., Kementzetzidis, E., Tsetas,
980 A., Molenkamp, T., van Beek, K. & P. D. (2020). Gdp: a new
981 technology for gentle driving of (mono)piles. In *Frontiers in*
982 *Offshore Geotechnics IV: Proceedings of the 4th International*
983 *Symposium on Frontiers in Offshore Geotechnics (ISFOG 2021)*. 984
- Nicolai, G. & Ibsen, L. B. (2014). Small-scale testing of cyclic laterally
985 loaded monopiles in dense saturated sand. *Journal of Ocean and*
986 *Wind Energy* **1**, No. 4, 240–245. 987
- Niemunis, A., Wichtmann, T. & Triantafyllidis, T. (2005). A high-
988 cycle accumulation model for sand. *Computers and geotechnics* **32**,
989 No. 4, 245–263. 990
- Page, A. M., Klinkvort, R. T., Bayton, S., Zhang, Y. & Jostad,
991 H. P. (2020). A procedure for predicting the permanent rotation
992 of monopiles in sand supporting offshore wind turbines. *Marine*
993 *Structures* **75**, 102813. 994
- Page, A. M., Næss, V., De Vaal, J. B., Eiksund, G. R. & Nygaard, T. A.
995 (2019). Impact of foundation modelling in offshore wind turbines:
996 Comparison between simulations and field data. *Marine Structures*
997 **64**, 379–400. 998
- Park, J. & Santamarina, J. (2019). Sand response to a large number
999 of loading cycles under zero-lateral-strain conditions: evolution of
1000 void ratio and small-strain stiffness. *Géotechnique* **69**, No. 6, 501–
1001 513. 1002
- Pisanò, F. (2019). Input of advanced geotechnical modelling to the
1003 design of offshore wind turbine foundations. In *Proceedings of the*
1004 *17th European Conference on Soil Mechanics and Geotechnical*
1005 *Engineering (ECSMGE 2019)*, International Society of Soil 1006

- 1007 Mechanics and Geotechnical Engineering.
- 1008 Richards, I., Bransby, M., Byrne, B., Gaudin, C. & Houlsby, G.
1009 (2021). Effect of stress level on response of model monopile
1010 to cyclic lateral loading in sand. *Journal of Geotechnical and*
1011 *Geoenvironmental Engineering* **147**, No. 3, 04021002.
- 1012 Richards, I. A. (2019). *Monopile foundations under complex cyclic*
1013 *lateral loading*. Ph.D. thesis, University of Oxford.
- 1014 Richards, I. A., Byrne, B. W. & Houlsby, G. T. (2019). Monopile
1015 rotation under complex cyclic lateral loading in sand. *Géotechnique*
1016 , Ahead of print.
- 1017 Rudolph, C., Bienen, B. & Grabe, J. (2014). Effect of variation of
1018 the loading direction on the displacement accumulation of large-
1019 diameter piles under cyclic lateral loading in sand. *Canadian*
1020 *Geotechnical Journal* **51**, No. 10, 1196–1206.
- 1021 Scott, M. H. & Fenves, G. L. (2003). A krylov subspace accelerated
1022 newton algorithm. In *2003 ASCE/SEI Structures Congress and*
1023 *Exposition: Engineering Smarter*.
- 1024 Sheil, B. B. & McCabe, B. A. (2017). Biaxial loading of
1025 offshore monopiles: numerical modeling. *International Journal of*
1026 *Geomechanics* **17**, No. 2, 04016050.
- 1027 Sloan, S. W. (1987). Substepping schemes for the numerical integration
1028 of elastoplastic stress–strain relations. *International journal for*
1029 *numerical methods in engineering* **24**, No. 5, 893–911.
- 1030 Sloan, S. W., Abbo, A. J. & Sheng, D. (2001). Refined explicit
1031 integration of elastoplastic models with automatic error control.
1032 *Engineering Computations* **18**, No. 1/2, 121–194.
- 1033 Staubach, P., Machaček, J., Moscoso, M. & Wichtmann, T. (2020).
1034 Impact of the installation on the long-term cyclic behaviour of
1035 piles in sand: A numerical study. *Soil Dynamics and Earthquake*
1036 *Engineering* **138**, 106223.
- 1037 Staubach, P. & Wichtmann, T. (2020). Long-term deformations of
1038 monopile foundations for offshore wind turbines studied with a
1039 high-cycle accumulation model. *Computers and Geotechnics* **124**,
1040 103553.
- 1041 Tabora, D. M., Zdravković, L., Potts, D. M., Burd, H. J., Byrne, B. W.,
1042 Gavin, K. G., Houlsby, G. T., Jardine, R. J., Liu, T., Martin, C. M.
1043 *et al.* (2019). Finite-element modelling of laterally loaded piles in
1044 a dense marine sand at dunkirk. *Géotechnique* , Ahead of print.
- 1045 Tamagnini, C., Viggiani, G., Chambon, R. & Desrues, J. (2000).
1046 Evaluation of different strategies for the integration of hypoplastic
1047 constitutive equations: Application to the cloe model. *Mechanics*
1048 *of Cohesive-frictional Materials: An International Journal on*
1049 *Experiments, Modelling and Computation of Materials and*
1050 *Structures* **5**, No. 4, 263–289.
- 1051 Truong, P., Lehane, B. M., Zania, V. & Klinkvort, R. T. (2019).
1052 Empirical approach based on centrifuge testing for cyclic
1053 deformations of laterally loaded piles in sand. *Géotechnique* **69**,
1054 No. 2, 133–145, doi:10.1680/jgeot.17.P.203.
- 1055 Tsai, Y.-C., Huang, Y.-F. & Yang, J.-T. (2016). Strategies for the
1056 development of offshore wind technology for far-east countries–
1057 a point of view from patent analysis. *Renewable and Sustainable*
1058 *Energy Reviews* **60**, 182–194.
- 1059 Tsuha, C. d. H., Foray, P., Jardine, R., Yang, Z. X., Silva, M. & Rimoy,
1060 S. (2012). Behaviour of displacement piles in sand under cyclic
1061 axial loading. *Soils and foundations* **52**, No. 3, 393–410.
- 1062 Wichtmann, T. (2005). *Explicit accumulation model for non-cohesive*
1063 *soils under cyclic loading*. Ph.D. thesis, Inst. für Grundbau und
1064 Bodenmechanik Bochum University, Germany.
- Wichtmann, T., Triantafyllidis, T., Chrisopoulos, S., Zachert, H. 1065
et al. (2017). Prediction of long-term deformations of offshore 1066
wind power plant foundations using HCA-based engineer-oriented 1067
models. *International Journal of Offshore and Polar Engineering* 1068
27, No. 04, 346–356. 1069